CHEMISTRY
A EUROPEAN JOURNAL

DOI: 10.1002/chem.201001132

VIP

Hydration Preferences for Mn_4Ca Cluster Models of Photosystem II: Location of Potential Substrate–Water Binding Sites

Simon Petrie, Rob Stranger,* and Ron J. Pace[a]

Abstract: Density functional theory calculations are reported on a set of three model structures of the Mn_4Ca cluster in the water-oxidizing complex of Photosystem II (PSII), which share the structural formula $[CaMn_4C_9H_{10}N_2O_{16}]^{q+}\cdot(H_2O)_n$ ($q=-1$, 0, 1, 2, 3; $n=0$–7). In these calculations we have explored the preferred hydration sites of the Mn_4Ca cluster across five overall oxidation states (S_0 to S_4) and all feasible magnetic-coupling arrangements to identify the most likely substrate–water binding sites. We have also explored charge-compensated structures in which the overall charge on the cluster is maintained at $q=0$ or $+1$, which is consistent with the experimental data on sequential proton loss in the real system. The three model structures have skeletal arrangements that are strongly reminiscent, in their relative metal-atom positions, of the 2.9-, 3.7-, and 3.5 Å-resolution crystal structures, respectively, whereas the charge states encompassed in our study correspond to an assignment of $(Mn^{III})_3Mn^{II}$ for S_0 and up to $(Mn^{IV})_3Mn^{III}$ for S_4. The three models differ principally in terms of the spatial relationship between one Mn (Mn(4)) and a generally robust Mn_3Ca tetrahedron that contains Mn(1), Mn(2), and Mn(3). Oxidation-state distributions across the four manganese atoms, in most of the explored charge states, are dependent on details of the cluster geometry, on the extent of assumed hydration of the clusters, and in some instances on the imposed magnetic-coupling between adjacent Mn atoms. The strongest water-binding sites are generally those on Mn(4) and Ca. However, one structure type displays a high-affinity binding site between Ca and Mn(3), the S-state-dependent binding-energy pattern of which is most consistent with the substrate water-exchange kinetics observed in functional PSII. This structure type also permits another water molecule to access the cluster in a manner consistent with the substrate–water interaction with the Mn cluster, seen in electron spin-echo envelope modulation (ESEEM) studies of the functional enzyme in the S_0 and S_2 states. It also rationalizes the significant differences in hydrogen-bonding interactions of the substrate water observed in the FTIR measurements of the S_1 and S_2 states. We suggest that these two water-binding sites, which are molecularly close, model the actual substrate-binding sites in the enzyme.

Keywords: density functional calculations · metalloproteins · mixed-valent compounds · photosystem II · water chemistry

Introduction

Water is the substrate for production of molecular oxygen in Photosystem II (PSII), a process for which the precise mechanistic details remain enigmatic. What is known is that, during the cyclic four-electron process of water oxidation, the Mn_4Ca cluster in the water-oxidizing complex (WOC) of PSII moves through a series of four metastable, spectroscopically accessible intermediate states and one intrinsically shortlived unstable state, collectively known as the S states. Electron transfer from the cluster takes place by means of a redox-active tyrosine residue, Y_z. The metastable states are labeled S_0, S_1, S_2, and S_3, and the shortlived 'final' state is S_4, for which the subscript refers to the number of stored oxidizing equivalents in the catalytic center.[1] However, the geometry of the Mn_4Ca site of the WOC, and indeed the overall metal-center oxidation state at which water oxidation occurs, are still the subject of vigorous debate.

A large component of the challenge in unraveling the mechanism of water oxidation lies in the difficulty of unambiguous characterization of the active-site geometry. Several medium-resolution crystal structures have been reported, at

[a] Dr. S. Petrie, Prof. R. Stranger, Prof. R. J. Pace
Research School of Chemistry, Australian National University
Canberra, ACT 0200 (Australia)
Fax: (+61) 2 61250760
E-mail: rob.stranger@anu.edu.au

Supporting information for this article is available on the WWW under http://dx.doi.org/10.1002/chem.201001132.

progressively 3.8, 3.7, 3.5, 3.2, 3.0,[2–6] and very recently, 2.9 Å resolution,[7] but although these structures bear common features—notably a tight triangular arrangement of three of the four manganese atoms in the WOC—there is considerable disparity between the assigned positions of one of the Mn atoms, and of the ligating protein residues, in the various XRD-derived geometries. Further structural information has been obtained from extended X-ray absorption fine structure (EXAFS) and other techniques,[8] in some instances drawing on the crystal-structure results; but it has been argued that the PSII active site is highly susceptible to X-ray-induced damage, and that this damage is the source of apparent discrepancies between the crystal structures.[9] It is fair to say that there is still no universally accepted geometry for the PSII active site, despite exhaustive investigation by many research groups.

We have previously suggested[10,11] that the various crystal-structure geometries might be straightforwardly interrelated. This inference arises because calculations on a series of isomeric oxo-bridged Mn_4Ca-containing clusters,[10,11] with surrounding carboxylate ligands arranged in a manner consistent with the most recent 3.0- and 2.9 Å-resolution ('Berlin') crystal structures,[6,7] reveal that these isomers can undergo interconversion between forms whose metal-atom positions are strikingly reminiscent of the Mn_4 geometries of the 3.7 Å 'Hyogo,'[3] 3.5 Å 'London,'[5] and 2.9 Å 'Berlin'[6,7] crystal structures. Such interconversion, if real in the protein, might even occur prior to X-ray exposure, during the chemical workup needed to extract and crystallize the PSII complex.

Given the challenges that confront laboratory characterization of the atomic-level structure of the active site of PSII, there is a strong need for complementary approaches to PSII structure determination. Computational chemistry is one such avenue, and has already been adopted to this end by several research groups over the past few years. Siegbahn and co-workers have performed an extensive set of density functional theory (DFT) calculations on a PSII model[12–20] derived principally from the 3.5 Å resolution 'London' XRD structure.[5] A further in-depth DFT computational investigation, including solvent corrections and an ONIOM (our own *n*-layered integrated molecular orbital and molecular mechanics) treatment of the surrounding protein environment, has been undertaken by Batista et al.,[21–26] whereas Kusunoki[27] has reported the results of DFT calculations on a model based on the 3.0 Å 'Berlin' XRD structure.[6] Although there are several differences between the various PSII models in the aforementioned computational studies, one important common starting point is the assignment of a $Mn^{III}(Mn^{IV})_3$ oxidation-state pattern to the S_2 state of PSII.

Our own computational explorations of the PSII active site have taken a different tack. Based on comparison with S-state-dependent EXAFS distances, we favor an oxidation-state assignment of $(Mn^{III})_3Mn^{IV}$ as the S_2 state.[11] Further, we have sought to canvas a wider distribution of possible structures, by investigating various Mn_4Ca geometries—reminiscent, as noted above, of each of the Berlin,[6] London,[5] and Hyogo[3] crystal structures in terms of their respective metal-atom positions—across a range of five charge states, and investigating all feasible single-determinant magnetic-coupling configurations of the four Mn atoms for each structure type **I** ('Berlin-like'), **II** ('Hyogo-like'), and **III** ('London-like'). Our initial DFT study on three $[CaMn_4C_9H_{10}N_2O_{16}]^{+\bullet}\cdot 3H_2O$ isomers indicated that these three structure types displayed comparatively facile interconversion.[10] A subsequent investigation of trihydrated $[CaMn_4C_9H_{10}N_2O_{16}]^{q+}$ ($q=-1$ to $+3$)[11] revealed generally dissimilar oxidation-state patterns between **I**, **II**, and **III** for any given charge state (although the assumed S_1 structures, with $q=0$, all adopted a $Mn^{III}Mn^{IV}Mn^{III}Mn^{II}$ ('3432') oxidation-state pattern), and a propensity towards antiferromagnetic interactions between neighboring Mn atoms, particularly in the assigned lower S-state structures.

The optimized arrangement of ligands that model the protein groups in the Berlin-like **I** structure is close to that resolved in the actual 3.0 and 2.9 Å Berlin XRD structures.[6,7] For Hyogo-like **II**, the calculated ligand orientation is broadly consistent with the reported Hyogo XRD structure,[3] within the limits of the 3.7 Å resolution obtained in the latter study. For the London-like **III** cluster, the relative metal positions closely match those seen in the London XRD structure,[5] but the ligand positions seen both experimentally[5] and by quantum mechanics/molecular mechanics (QM/MM) simulations[24] are somewhat different from our model arrangement in which all the carboxylate groups bind and/or bridge in a generally equivalent manner in the three computational clusters studied here. As a consequence, QM/MM modeling of the London structure[24] suggests that water molecules are present in places excluded in our current studies, particularly for Mn(2), whereas other sites possible in our model structures (e.g., on Mn(1)) are excluded (see Figure 1 and ref. [6] for Mn numbering).

Within our set of model structures, hydration at Mn(4) and Ca—which are left coordinatively unsaturated by ligation of the surrounding protein environment—is possible, whereas the opportunity for hydration at Mn(1) or Mn(3) is dependent upon the geometry of the metal-atom cluster. Hydration at Mn(2) cannot occur due to the local octahedral coordination of protein-based donor atoms and O bridges at this atom. Our calculations on trihydrated models[11] uncovered many examples of Mn(4)- and Ca-hydrated structures, and some instances of hydration at Mn(1) or Mn(3) (as well as a surprising tendency for water molecules to occupy the second solvation layer in apparent preference over primary coordination to a metal atom), but left unanswered the points of attachment for the substrate water molecules central to the mechanism of PSII water oxidation.

In the calculations reported here, we have explored the consequences of sequential hydration (up to 7 water ligands) on our series of Mn_4Ca structure types across charge states from $q=-1$ to $q=+3$. This affords considerable detail on the influence of hydration on our PSII models. In addition, we have also performed calculations on relevant charge-compensated structures with $q=0$ or $+1$ so that the overall

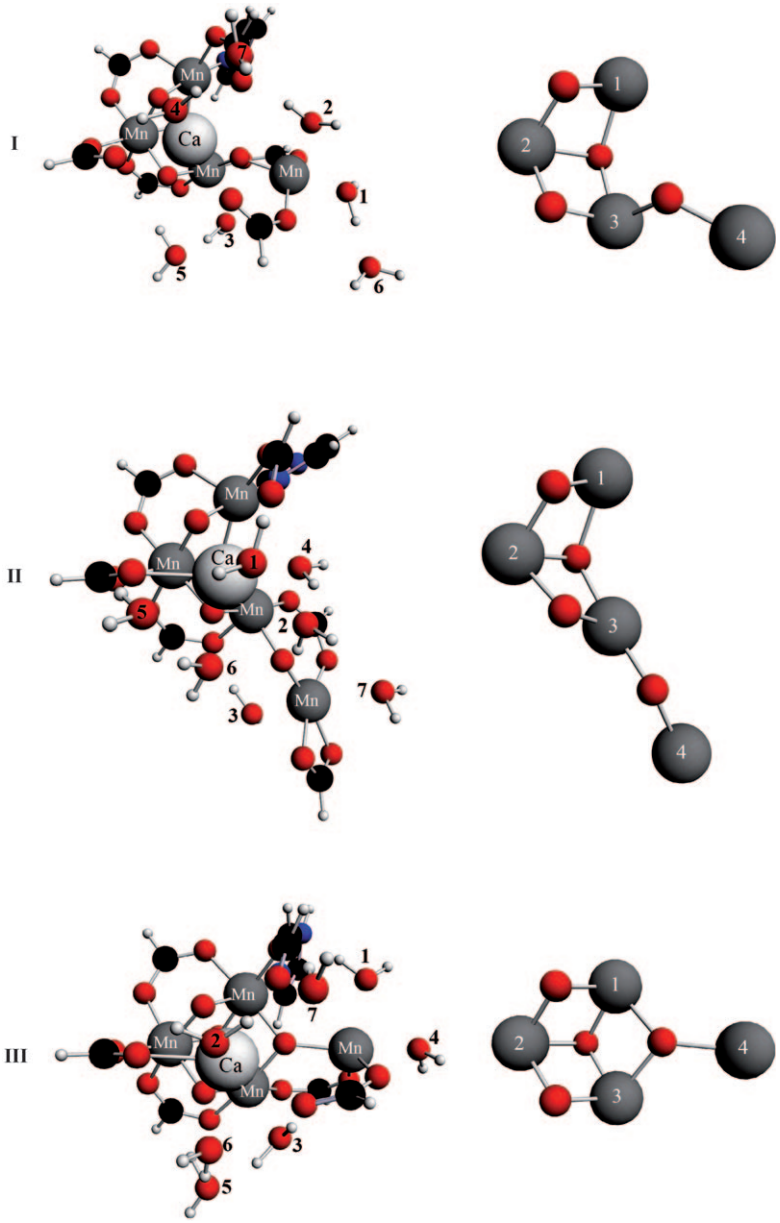

Figure 1. Structures of the lowest-energy heptahydrated complexes of clusters **I**, **II**, and **III**, each in the dicationic charge state. Structures are viewed along a line-of-sight nearly coincident with the axis passing down through Ca to the tri-μ-oxo bridge that links Mn(1), Mn(2), and Mn(3), with Mn(1) oriented approximately north, and Mn(2) due west, of the projected Ca atom. The diagrams are annotated with the hierarchies of water-ligand attachment, with '1' indicating the strongest-bound water ligand.

charge on the cluster remains consistent with the proton-loss sequence observed in experimental studies. When assessed against recent experimental data that relates to substrate–water interaction with the WOC, the calculations provide valuable information on the relevance of these structure types for the cluster geometry in catalytically active PSII and, importantly, the location of potential substrate–water binding sites.

Results and Discussion

First, we summarize the results of our calculations on the variously hydrated Mn_4Ca cluster models **I, II**, and **III** (see Figure 1) across the −1 to +3 charge states that correspond, in formal Mn oxidation levels, to our S_0 to S_4 states. Subsequent sections of the discussion address results from these and related charge-compensated species, with reference to experimental data on substrate–water binding and interaction with the water-oxidizing complex of PSII.

Influence of hydration on metal-oxidation states and magnetic-coupling modes: An extensive survey of the Mn_4Ca cluster model structures as a function of charge state, hydration level, and magnetic coupling mode has been made. These data are summarized in two series of tables within the Supporting Information that accompanies this work. Tables S1 to S15 detail the crucial metal–metal distances as a stepwise function of hydration level for each structure of type **I**, **II**, and **III** across the charge states $q=-1$ to +3. The magnetic character of the heptahydrated models is summarized in Tables 1 to 5 below, with a more exhaustive overview (explored at the $n=0$, 3, and 7 hydration levels) provided in Tables S16 to S30, again within the Supporting Information. In the discussion below, we focus on the results from Tables 1 to 5, with some references as appropriate to the Supporting Information.

The −1 charge state: The −1 charge state (see Table 1), which corresponds to $(Mn_4)^{11+}Ca^{2+}(O^{2-})_4(OCHO^-)_6(c\text{-}C_3H_4N_2)(H_2O)_n$, models the WOC S_0 state, effectively $Mn^{II}(Mn^{III})_3$ or its formal equivalent. For this charge state, three competing oxidation-state patterns are manifested in the various models: $Mn^{III}Mn^{III}Mn^{III}Mn^{II}$ (henceforth '3332'), $Mn^{II}Mn^{IV}Mn^{III}Mn^{II}$ ('2432'), and $Mn^{III}Mn^{IV}Mn^{II}Mn^{II}$ ('3422'). Of the three overall Mn_4Ca cluster structure types

Table 1. Trends in total and relative energies, and Mn-atom spin densities, of ferromagnetically coupled and low-lying antiferromagnetically coupled configurations of the structures $\mathbf{I}^{-1}\cdot(H_2O)_7$, $\mathbf{II}^{-1}\cdot(H_2O)_7$, and $\mathbf{III}^{-1}\cdot(H_2O)_7$ as a function of magnetic coupling.

Coupling scheme[a]		M_S[b]	E_{tot}[c] [hartree]	E_{rel}[d] [kJ mol^{-1}]	$\mu_{spin}(1)$[e]	$\mu_{spin}(2)$[e]	$\mu_{spin}(3)$[e]	$\mu_{spin}(4)$[e]
			$\mathbf{I}^{-1}\cdot(H_2O)_7$: ($Mn^{III}/Mn^{III}/Mn^{III}/Mn^{II}$)					
AAAA	FFF	+17/2	−14.42970	28 (29)	3.8532	3.8698	3.7847	4.8081
AABA	FAA	+9/2	−14.43681	9 (10)	3.6570	3.8432	−3.4751	4.6656
ABBA	AFA	+3/2	−14.43701	8 (9)	*3.7359*	*−2.1396*	*−3.4141*	*4.6368*
ABBA	AFA	+1/2	−14.43895	3 (4)	3.6387	−3.8023	−3.4947	4.6546
ABAB	AAA	−1/2	−14.44019	0 (1)	3.8015	−3.7382	3.5576	−4.6481
			$\mathbf{II}^{-1}\cdot(H_2O)_7$: ($Mn^{II}/Mn^{IV}/Mn^{III}/Mn^{II}$)					
AAAA	FFF	+17/2	−14.42343	45	4.7732	2.8517	3.8969	4.8394
ABBB	AFF	−9/2	−14.43681	10	*3.6628*	*−3.8135*	*−3.7546*	*−4.8385*
ABAB	AAA	+1/2	−14.43874	5	4.5394	−2.6078	3.7692	−4.7534
AABA	FAA	+9/2	−14.44060	0	4.7855	2.7575	−3.6064	4.7314
			$\mathbf{III}^{-1}\cdot(H_2O)_7$: ($Mn^{III}/Mn^{IV}/Mn^{II}/Mn^{II}$)					
AAAA	FFF	+17/2	−14.41612	54 (64)	3.8269	2.8615	4.7981	4.8390
ABAB	AAA	+1/2	−14.43186	13 (23)	3.7269	−2.5699	4.6264	−4.7457
ABAA	AAF	+9/2	−14.43676	0 (10)	*2.7387*	*−3.6716*	*4.7805*	*4.7882*

[a] The four-character identifier shows the constrained preference of each of the four Mn atoms for alpha- (A) or beta- (B) spin valence d-electron density. Thus, 'AABA' indicates the coupling pattern in which Mn atoms 1, 2, and 4 have α-spin electron-density excess, whereas Mn-atom 3 has β-spin excess. The three-character identifier denotes the mode of coupling between sequential Mn atoms (treating the complex as a linear Mn chain, which may not be strictly valid), as either antiferromagnetic (A) or ferromagnetic (F). Thus, 'FAA' shows that the coupling between Mn atoms 1 and 2 is ferromagnetic, whereas the coupling between 2 and 3, as well as between 3 and 4, is antiferromagnetic. Identifiers shown in italics indicate a pattern of Mn oxidation states noticeably at variance with that delivered by calculation on the fully ferromagnetic 'AAAA' configuration for the same structure. [b] Spin quantum number of the overall complex. [c] Calculated total ('bond') energy of the optimized complex in the indicated spin configuration. [d] Calculated energy of the optimized complex in the indicated spin configuration, expressed relative to the lowest-energy configuration for this model at this overall oxidation state. Values in parentheses are expressed relative to the lowest-energy configuration of the lowest-energy structure (here, $\mathbf{II}^{-1}$). [e] Calculated spin density on the identified individual Mn atom. Values in italics indicate a pattern of Mn oxidation states noticeably at variance with that delivered by calculation on the fully ferromagnetic 'AAAA' configuration for the same structure.

that we have previously identified, the 'Berlin-like' geometry type **I** (characterized by an Mn(1)–Mn(4) distance of around 5.0 to 5.6 Å) is the lowest-energy structure, irrespective of the degree of hydration. It consistently exhibits a preference for the '3332' oxidation-state pattern and shows a preference for antiferromagnetic coupling, particularly the αββα (hereafter 'ABBA') $M_S=1/2$, ααβα (hereafter 'AABA') $M_S=9/2$, and αβαβ (hereafter 'ABAB') $M_S=-1/2$ coupling motifs.

Geometrically, the influence of hydration is consistent, regardless of the coupling pattern: addition of the first three water ligands results in a lengthening of the Mn(1)–Mn(4) distance by around 0.3–0.4 Å, whereas a further four hydration steps yield additional lengthening of this distance by a smaller increment, typically 0.1 Å or less.

The 'Hyogo-like' geometry **II**, typified by an Mn(1)–Mn(4) distance of 6.0 Å or greater, is more ambiguous than **I** with regards to its oxidation-state pattern preference. In the heptahydrate structure, the ferromagnetic configuration ('AAAA', $S=17/2$) is clearly '2432,' and all of the expected antiferromagnetic-coupling variants deliver unpaired Mn spin densities consistent with this oxidation-state pattern.

For lower hydration levels, the 3332 oxidation pattern is generally preferred, with the lowest energy states ($M_S=1/2$) similar in coupling to those of structure **I** (see Table S16 in the Supporting Information). For the ferromagnetically preferred '2432' oxidation-state pattern, hydration of **II** has a much smaller impact on the key Mn(1)–Mn(4) distance than is the case for geometry type **I**.

The 'London-like' geometry **III**, characterized by Mn(1)–Mn(4) separation of approximately 4.0 Å, also exhibits some oxidation-state pattern ambiguity. For the heptahydrate structure, the ferromagnetic 'AAAA' $S=17/2$ configuration is clearly '3422,' with a full complement of antiferromagnetic variants that also exhibit this oxidation-state pattern. For hydration levels $n=0$ and 3, the lowest-energy antiferromagnetic structures are both '3332' (ABAB $M_S=-1/2$ and AABA $M_S=9/2$, respectively) in preference to '3422' ABAB $M_S=1/2$. The geometric influence of hydration in **III** is largely to shorten the Mn(1)–Mn(4) distance, and it appears that hydration stabilizes this structure against spontaneous rearrangement to the generally lower-energy structure **I**.

The neutral charge state: The zero-charge state (see Table 2), which corresponds to $(Mn_4)^{12+}Ca^{2+}(O^{2-})_4(OCHO^-)_6(c\text{-}C_3H_4N_2)(H_2O)_n$, models the WOC S_1 state, effectively $(Mn^{III})_4$. In practice, however, although efforts were made to characterize structures with an $Mn^{III}Mn^{III}Mn^{III}Mn^{III}$ oxidation-state pattern (hereafter '3333'), no configurations of this type could be satisfactorily isolated. Instead, the type **I**, **II**, and **III** geometries all unambiguously adopted an $Mn^{III}Mn^{IV}Mn^{III}Mn^{II}$ ('3432') oxidation-state pattern.

Perhaps because they arise from this oxidation-state commonality across structures, the various geometries exhibit magnetic consistency in the sense that **I** prefers ABBA $M_S=1$ coupling, **II** favors ABAB $M_S=0$ and ABBA $M_S=1$, and **III** also opts for ABBA $M_S=1$; this is combined with a greater degree of structural fluidity than is seen in the −1

Table 2. Trends in total and relative energies, and Mn-atom spin densities, of ferromagnetically coupled and low-lying antiferromagnetically coupled configurations of the structures $\mathbf{I}^0\cdot(H_2O)_7$, $\mathbf{II}^0\cdot(H_2O)_7$, and $\mathbf{III}^0\cdot(H_2O)_7$ as a function of magnetic coupling.

Coupling scheme[a]		M_S[a]	E_{tot}[a] [hartree]	E_{rel}[a,b] [kJ mol^{-1}]	$\mu_{spin}(1)$[a]	$\mu_{spin}(2)$[a]	$\mu_{spin}(3)$[a]	$\mu_{spin}(4)$[a]
			$\mathbf{I}^0\cdot(H_2O)_7$: ($Mn^{III}/Mn^{IV}/Mn^{III}/Mn^{II}$)					
AAAA	FFF	+8	14.34884	7 (12)	3.8566	2.8768	3.8270	4.8277
AABA	FAA	+4	14.34730	11 (16)	3.7693	2.8594	−3.6423	4.7441
ABAB	AAA	0	14.34900	6 (11)	3.7959	−2.7470	3.6698	−4.7387
ABBA	AFA	+1	14.35138	0 (5)	3.7341	−2.7759	−3.6893	4.7452
			$\mathbf{II}^0\cdot(H_2O)_7$: ($Mn^{III}/Mn^{IV}/Mn^{III}/Mn^{II}$)					
AAAA	FFF	+8	−14.32774	34 (67)	3.8235	2.9004	3.8735	4.8123
ABBA	AFA	+1	−14.33989	2 (35)	3.7484	−2.8067	−3.6158	4.6852
ABAB	AAA	0	−14.34057	0 (33)	3.7674	−2.7701	3.5983	−4.6746
			$\mathbf{III}^0\cdot(H_2O)_7$: ($Mn^{III}/Mn^{IV}/Mn^{III}/Mn^{II}$)					
AAAA	FFF	+8	−14.34164	30	3.8376	2.8750	3.8786	4.7980
ABBB	AFF	−4	−14.34946	10	3.6870	−2.7317	−3.8291	−4.7736
ABAB	AAA	0	−14.35100	6	3.7778	−2.7128	3.6065	−4.7266
ABBA	AFA	+1	14.35324	0	3.7240	−2.7431	−3.6577	4.7329

[a] For explanations of these parameters, refer to footnotes [a]–[e] of Table 1 . [b] Values in parentheses are expressed relative to the lowest-energy configuration of the lowest-energy structure (here, $\mathbf{III}^0$).

charge-state structures. Hydration has the contrasting effect of contracting the Mn(1)−Mn(4) separation in **III** while substantially increasing Mn(1)−Mn(4) in **II** and, to a lesser extent, in **I**.

The +1 charge state: The +1 charge state (see Table 3), which corresponds to $(Mn_4)^{13+}Ca^{2+}(O^{2-})_4(OCHO^-)_6(c\text{-}C_3H_4N_2)(H_2O)_n$, models the WOC S_2 state, effectively $(Mn^{III})_3Mn^{IV}$ or its formal equivalent. Although all the monocationic structures correspond to $(Mn^{III})_3Mn^{IV}$, only Mn(2) is seen to be fixed in oxidation state—at Mn^{IV}—across all structure types and hydration levels, with Mn(1) and Mn(3) toggling between Mn^{III} and Mn^{IV}, and Mn(4) varying between Mn^{II} and Mn^{III}. In structure type **I**, hydration has the effect of contracting the Mn(1)−Mn(4) distance—the opposite effect to that seen for $\mathbf{I}^0$ as discussed above—while also influencing the preferred oxidation-state pattern. Among 'genuine' anhydrous Berlin-like geometries, the lowest-energy configuration is ABBA $M_S=1/2$ ($Mn^{III}Mn^{IV}Mn^{III}Mn^{III}$, '3433'), which is also the preferred mode of magnetic coupling in the trihydrated condition. Further hydration to the heptahydrate changes the oxidation-state pattern preference to $Mn^{III}Mn^{IV}Mn^{IV}Mn^{II}$ ('3442'), for which three magnetic-coupling options, ABBA $M_S=3/2$, ABAB $M_S=-1/2$, and AAAB $M_S=5/2$ are almost isoenergetic.

For Hyogo-like $\mathbf{II}^+$, hydration has a negligible effect on the key Mn(1)−Mn(4) distance, with the preferred oxidation-state pattern, '3433,' also being essentially invariant. The magnetic coupling for this species, however, is less

Table 3. Trends in total and relative energies, and Mn-atom spin densities, of ferromagnetically coupled and low-lying antiferromagnetically coupled configurations of the structures $\mathbf{I}^{+1}\cdot(H_2O)_7$, $\mathbf{II}^{+1}\cdot(H_2O)_7$, and $\mathbf{III}^{+1}\cdot(H_2O)_7$ as a function of magnetic coupling.

Coupling scheme[a]		M_S[a]	E_{tot}[a] [hartree]	E_{rel}[a,b] [kJ mol^{-1}]	$\mu_{spin}(1)$[a]	$\mu_{spin}(2)$[a]	$\mu_{spin}(3)$[a]	$\mu_{spin}(4)$[a]
			$\mathbf{I}^{+1}\cdot(H_2O)_7$: ($Mn^{III}/Mn^{IV}/Mn^{IV}/Mn^{II}$)					
AAAA	FFF	+15/2	14.12843	26 (46)	3.8513	2.8716	2.9386	4.7882
AABA	FAA	+9/2	14.13490	9 (29)	3.8153	2.8622	2.5256	4.6132
AAAB	FFA	+5/2	14.13757	2 (22)	3.8343	2.8537	2.6316	4.6230
ABAB	AAA	−1/2	−4.13813	0.03 (21)	3.8077	2.7794	2.6109	4.6272
ABBA	AFA	+3/2	14.13819	0 (21)	3.7878	2.7816	2.5539	4.6219
			$\mathbf{II}^{+1}\cdot(H_2O)_7$: ($Mn^{III}/Mn^{IV}/Mn^{III}/Mn^{III}$)					
AAAA	FFF	+15/2	14.12639	35 (52)	3.8567	2.9130	3.8250	3.8940
ABBB	AFF	−7/2	−4.13968	0.4 (17)	3.7670	2.8282	3.7859	3.8877
AABB	FAF	−1/2	−4.13985	0 (16)	3.8121	2.8303	3.7358	3.8849
			$\mathbf{III}^{+1}\cdot(H_2O)_7$: ($Mn^{IV}/Mn^{IV}/Mn^{III}/Mn^{II}$)					
AAAA	FFF	+15/2	14.13980	17	2.9493	2.8576	3.8982	4.7832
AABA	FAA	+7/2	14.14153	12	2.9261	2.7380	3.6816	4.7295
AABA	FAA	+9/2	14.14189	11	*3.7602*	*2.8826*	*2.4981*	*4.6135*
AAAB	FFA	+5/2	14.14231	10	2.7103	2.8512	3.8487	4.6943
ABAB	AAA	−1/2	−4.14303	8	2.7059	2.7566	3.7894	4.6994
ABBA	AFA	+1/2	−14.14304	8	2.8173	2.8330	3.7451	4.7242
AABB	FAF	−3/2	−14.14319	8	2.5978	2.7543	3.7508	4.7010
ABBA	AFA	+3/2	14.14611	0	*3.7099*	*2.7321*	*2.5363*	*4.6320*

[a] For explanations of these parameters, refer to footnotes [a]–[e] of Table 1. [b] Values in parentheses are expressed relative to the lowest-energy configuration of the lowest-energy structure (here, $\mathbf{III}^{+1}$).

Table 4. Trends in total and relative energies, and Mn-atom spin densities, of ferromagnetically coupled and low-lying antiferromagnetically coupled configurations of the structures $\mathbf{I}^{+2}\cdot(H_2O)_7$, $\mathbf{II}^{+2}\cdot(H_2O)_7$, and $\mathbf{III}^{+2}\cdot(H_2O)_7$ as a function of magnetic coupling.

Coupling scheme[a]		M_S[a]	E_{tot}[a] [hartree]	E_{rel}[a,b] [kJ mol^{-1}]	$\mu_{spin}(1)$[a]	$\mu_{spin}(2)$[a]	$\mu_{spin}(3)$[a]	$\mu_{spin}(4)$[a]
			$\mathbf{I}^{+2}\cdot(H_2O)_7$: ($Mn^{III}/Mn^{IV}/Mn^{IV}/Mn^{III}$)					
AAAA	FFF	+7	−13.81876	13 (19)	3.8237	2.8706	2.9410	3.8570
ABAA	AAF	+4	−13.81990	10 (16)	3.7847	−2.7815	2.9219	3.8461
AABA	FAA	+4	−13.82083	7 (14)	3.7929	2.8698	−3.6748	3.7990
ABBB	AFF	−3	−13.82095	7 (13)	3.7521	−2.7971	−2.7941	−3.8308
AAAB	FFA	+3	−13.82140	6 (12)	3.8312	2.8693	2.8214	−3.7816
ABBA	AFA	+1	−13.82356	0 (6)	3.7502	−2.7894	−2.6849	3.8059
			$\mathbf{II}^{+2}\cdot(H_2O)_7$: ($Mn^{III}/Mn^{IV}/Mn^{IV}/Mn^{III}$)					
AAAA	FFF	+7	−13.80451	22 (56)	3.8192	2.8718	2.8702	3.8979
ABAB	AAA	0	−13.81015	7 (42)	3.7602	−2.7695	2.6979	−3.7970
AABB	FAF	−1	−13.81052	6 (41)	*2.7331*	*2.7865*	*−3.7442*	*−3.9114*
ABBA	AFA	+1	−13.81092	5 (40)	3.7534	−2.7903	−2.5777	3.8084
AABA	FAA	+4	−13.81110	4 (39)	3.7876	2.8562	−2.5338	3.8109
AABA	FAA	+3	−13.81275	0 (35)	2.7416	2.7891	−3.6474	3.8182
			$\mathbf{III}^{+2}\cdot(H_2O)_7$: ($Mn^{IV}/Mn^{IV}/Mn^{IV}/Mn^{II}$)					
AAAA	FFF	+7	−13.81477	30	3.0456	2.8404	2.9852	4.6658
ABAA	AAF	+4	−13.82213	10	3.1197	−2.8204	3.0157	4.5548
ABBB	AFF	−4	−13.82261	9	2.6722	−2.8290	−2.9307	−4.7033
AABB	FAF	−1	−13.82290	8	2.6699	2.8400	−2.9112	−4.7180
ABBA	AFA	+1	−13.82530	2	2.9646	−2.8329	−2.7171	4.6362
AABA	FAA	+4	−13.82553	1	2.9607	2.8428	−2.6936	4.6470
AAAB	FFA	+2	−13.82601	0	2.7417	2.8255	2.7362	−4.6303

[a] For explanations of these parameters, refer to footnotes [a]–[e] of Table 1. [b] Values in parentheses are expressed relative to the lowest-energy configuration of the lowest-energy structure (here, $\mathbf{III}^{+2}$).

clear. In the anhydrous form, four low-lying coupling modes—AABA $M_S=7/2$, ABBA $M_S=1/2$, AABB $M_S=-1/2$, and ABAB $M_S=1/2$—are too close energetically to unambiguously assign a preferred configuration. Addition of three water molecules resolves the picture somewhat, with only two coupling modes—AABA $M_S=7/2$ and ABBA $M_S=1/2$—competing for the lowest-energy configuration, whereas in the heptahydrated system the preferred coupling modes are AABB $M_S=-1/2$ and ABBB $M_S=-7/2$.

For London-like $\mathbf{III}^{+}$, the oxidation-state preference is primarily towards '4432' (with AABA $M_S=7/2$ and ABBA $M_S=1/2$ coupling the lowest-energy modes in the anhydrous state, and AABA $M_S=7/2$ on trihydration). In the heptahydrate, the lowest-energy configuration is ABBA $M_S=3/2$ ('3442'). One unusual aspect of the results for $\mathbf{III}^{+}$ is that there are three distinct plausible oxidation-state patterns for which single-determinant magnetic-coupling configurations can be satisfactorily characterized, namely, 4432, 3442, and 3433, with representatives of each oxidation-state pattern lying within 30 kJ mol^{-1} of the lowest-energy coupling mode at each of the anhydrous, trihydrated, and heptahydrated conditions.

In this charge state, interconversion between structure types is more effectively impeded than is the case for the charge-neutral structures discussed above. Interconversion between $\mathbf{I}^{+}$ and $\mathbf{III}^{+}$ is seen in only a few instances, and generally only for the anhydrous (or, occasionally, trihydrated) cases. The 'Hyogo-like' structure $\mathbf{II}^{+}$ is particularly resistant to structural rearrangement, in contrast with the charge-neutral system in which anhydrous **II** adopts a structure quite similar to 'Berlin-like' **I**.

The +2 charge state: The +2 charge state (see Table 4), which corresponds to $(Mn_4)^{14+}Ca^{2+}(O^{2-})_4(OCHO^{-})_6(c\text{-}C_3H_4N_2)(H_2O)_n$, models the WOC S_3 state, effectively $(Mn^{III})_2(Mn^{IV})_2$ or its formal equivalent. Whereas the dicationic models (see Table 4) generally correspond to a tetramanganese combination of $(Mn^{III})_2(Mn^{IV})_2$, other patterns of oxidation states also occur among the structures explored here. Berlin-like $\mathbf{I}^{2+}$ has ABAB $M_S=0$ as its lowest-energy coupling mode in the anhydrous structure. This can be assigned as the $Mn^{III}Mn^{IV}Mn^{IV}Mn^{III}$ oxidation-state pattern ('3443'), which is also the oxidation-state pattern preferred among the trihydrated and heptahydrated species. The effect of hydration is to constrain the preferred oxidation-state pattern as 3443. Concomitant with this adjustment, the geometry transforms itself through a considerable shortening of the Mn(1)−Mn(4) distance, from typically around 5.3 Å in the anhydrous case to around 4.3 Å in the heptahydrated case.

The same oxidation-state ambivalence seen in anhydrous $\mathbf{I}^{2+}$ can be discerned across the anhydrous and trihydrated versions of $\mathbf{II}^{2+}$. The fully ferromagnetically coupled AAAA $S=7$ has manganese spin densities indicative of an oxidation-state pattern intermediate between 3443 and 4433, though leaning more towards 3443. In the heptahydrated version, the ferromagnetically coupled AAAA $S=7$ adopts an oxidation-state pattern that is unambiguously 3443. In both the anhydrous and heptahydrated cases, the lowest-energy coupling patterns are representative of '4433,' namely, ABBB $M_S=-4$ in the anhydrous case, and heptahydrated AABA $M_S=3$, whereas in the trihydrated case the preferred coupling mode is ABAB $M_S=0$, which has a spin-density distribution intermediate between 3443 and 4433.

For London-like $\mathbf{III}^{2+}$, the fully ferromagnetic configuration AAAA $S=7$ consistently leans towards a '4442' oxidation pattern, and for both the anyhdrous and heptahydrated cases, the lowest antiferromagnetically coupled configurations (ABBA $M_S=1$, AAAB $M_S=2$, and AABA $M_S=4$) all have unambiguous '4442' oxidation states. However, the trihydrated species displays a preference for the '3443' oxidation state, with the three lowest antiferromagnetic coupling schemes, AAAB $M_S=3$, AABB $M_S=0$, and ABAB $M_S=0$ all showing this oxidation-state pattern. There is also an increased tendency towards structural interconversion of $\mathbf{III}^{2+}$ to $\mathbf{I}^{2+}$ on moderate hydration, since the Mn(1)–Mn(4) distance for the lowest-energy trihydrated coupling modes is consistently considerably larger than for the other configurations of $\mathbf{III}^{2+}$.

The +3 charge state: The +3 charge state (see Table 5), which corresponds to $(Mn_4)^{15+}Ca^{2+}(O^{2-})_4(OCHO^-)_6(c\text{-}C_3H_4N_2)(H_2O)_n$, models the WOC S_4 state, effectively $Mn^{III}(Mn^{IV})_3$ or its formal equivalent. The trihydrated models (see Table 5) are representative of $Mn^{III}(Mn^{IV})_3$ complexes, and all of the structures surveyed conform generally to this oxidation-state pattern. For $\mathbf{I}^{3+}$, the only oxidation-state pattern isolable with any reliability is $Mn^{IV}Mn^{IV}Mn^{IV}Mn^{III}$ ('4443'). The AABA $M_S=7/2$ and ABBA $M_S=1/2$ modes are consistently among the lowest-energy coupling modes across the range of hydration levels, although in the trihydrated state the lowest-energy coupling configuration is ABAB $M_S=-1/2$. Systematic contraction of the Mn(1)–Mn(4) distance is evident on hydration, although none of the species characterized from an initial $\mathbf{I}^{3+}$ geometry showed any tendency to undergo conversion to $\mathbf{III}^{3+}$.

The preferred oxidation-state pattern in the hydrated form of $\mathbf{II}^{3+}$ is $Mn^{IV}Mn^{IV}Mn^{III}Mn^{IV}$ ('4434'), consistent with the AABA $M_S=7/2$ mode, which is lowest-energy for both the trihydrated and heptahydrated cases, although for the anhydrous structure the lowest in energy antiferromagnetic coupling mode (ABAB $M_S=-1/2$) and the ferromagnetically coupled AAAA $S=13/2$ state are both identifiably '4443'. Mn(1)–Mn(4) distances for this structure type are not greatly influenced by hydration.

The heptahydrated form of $\mathbf{III}^{3+}$, which throughout its hydration levels manifests a preference for the '4443' oxidation-state pattern, has a markedly broader spin ladder than do the anhydrous and trihydrated versions. In heptahydrated $\mathbf{III}^{3+}$, the AAAA $S=13/2$ configuration is substantially higher in energy than the AABB $M_S=-1/2$, ABBA $M_S=1/2$ and ABBB $M_S=-7/2$ modes. As with $\mathbf{II}^{3+}$, there is very little influence of hydration on the key Mn(1)–Mn(4) distance.

Summary of trends: Overall, the models that we have explored can be described as weakly valence-trapped (with the charge-neutral system being the most notable example of relatively strong valence trapping, in the $Mn^{III}Mn^{IV}Mn^{III}Mn^{II}$ oxidation-state pattern). For the anionic and cationic charge states, the preferred oxidation-state pattern is subject to structural considerations and additionally influenced by hydration (and, sometimes, also by the mode of magnetic coupling). Mn(2), which is coordinatively saturated in the absence of any water ligation, has a propensity to exist as Mn^{IV} (and does so across at least four overall charge states, from zero to +3, regardless of structure type), whereas Mn(4), consistent with its relatively low anhydrous coordination number (3 in **I** and **III**, generally 4 in **II**), tends to persist as Mn^{II} into at least the neutral charge state (and to $q=+1$ for **III**). With coordinatively saturated Mn(2) adopting such a clear-cut stance on oxidation state, it is interesting to note that all the hydration-induced or structurally-influenced variation in manganese oxidation states occurs among just those Mn atoms—Mn(1), Mn(3), and Mn(4)—that do have the ability to coordinate water ligands, and which therefore encompass all the opportunities for Mn-centered water oxidation. With this in mind, it is obviously highly per-

Table 5. Trends in total and relative energies, and Mn-atom spin densities, of ferromagnetically coupled and low-lying antiferromagnetically coupled configurations of the structures $\mathbf{I}^{+3}\cdot(H_2O)_7$, $\mathbf{II}^{+3}\cdot(H_2O)_7$, and $\mathbf{III}^{+3}\cdot(H_2O)_7$ as a function of magnetic coupling.

Coupling scheme[a]		M_S[a]	E_{tot}[a] [hartree]	E_{rel}[a,b] [kJ mol^{-1}]	$\mu_{spin}(1)$[a]	$\mu_{spin}(2)$[a]	$\mu_{spin}(3)$[a]	$\mu_{spin}(4)$[a]
			$\mathbf{I}^{+3}\cdot(H_2O)_7$: ($Mn^{IV}/Mn^{IV}/Mn^{IV}/Mn^{III}$)					
AAAA	FFF	+13/2	−13.37354	32 (66)	2.8820	2.8243	2.8772	3.8725
ABAA	AAF	+7/2	−13.38241	9 (43)	2.8502	−2.7666	2.8555	3.8603
AABA	FAA	+7/2	−13.38545	1 (35)	2.8491	2.7989	−2.6454	3.7864
ABBA	AFA	+1/2	−13.38584	0 (34)	2.7741	−2.7995	−2.6759	3.7810
			$\mathbf{II}^{+3}\cdot(H_2O)_7$: ($Mn^{IV}/Mn^{IV}/Mn^{III}/Mn^{IV}$)					
AAAA	FFF	+13/2	−13.37003	25 (76)	2.8670	2.8765	3.8012	2.7835
AAAB	FFA	+5/2	−13.37670	7 (58)	*2.8101*	*2.8370*	*2.6183*	*−3.8135*
AAAB	FFA	+7/2	−13.37689	7 (58)	2.8680	2.8726	3.5926	−2.5574
AABA	FAA	+5/2	−13.37954	0 (51)	2.7578	2.8047	−3.5469	2.5764
			$\mathbf{III}^{+3}\cdot(H_2O)_7$: ($Mn^{IV}/Mn^{IV}/Mn^{IV}/Mn^{III}$)					
AAAA	FFF	+13/2	−13.39001	23	2.8986	2.8137	2.8430	3.8877
ABAA	AAF	+7/2	−13.39593	8	2.8754	−2.8109	2.8331	3.8741
ABBB	AFF	−7/2	−13.39813	2	2.7746	−2.8178	−2.8064	−3.8767
AABB	FAF	−1/2	−13.39816	2	2.7928	2.8185	−2.7971	−3.8655
ABBA	AFA	+1/2	−13.39883	0	2.8446	−2.8164	−2.7505	3.8566

[a] For explanations of these parameters, refer to footnotes [a]–[e] of Table 1. [b] Values in parentheses are expressed relative to the lowest-energy configuration of the lowest-energy structure (here, $\mathbf{III}^{+3}$).

tinent to explore the preferred water-binding sites for each structure at the various charge states, and this is discussed in the following section.

Hydration preferences as a function of structure type and charge state: Optimized geometries of the $\mathbf{I}^{2+}\cdot(H_2O)_7$, $\mathbf{II}^{2+}\cdot(H_2O)_7$, and $\mathbf{III}^{2+}\cdot(H_2O)_7$ heptahydrate structures, in the consistently antiferromagnetic 'ABAB' coupling pattern, are shown in Figure 1. Analogous geometries for the other charge states are presented in the Supporting Information. Within these structures, the water ligands are identified by a numerical hydration ranking, from 1 to 7, with 1 representing the strongest-bound, and 7 the weakest-bound, of the seven water ligands around each cluster. Note that the differences in optimized geometry and in hydration energy for different magnetic-coupling patterns have been found to be minimal. It should also be noted that in the 'London-like' structure type **III**, the presence of an additional tri-μ-oxo bridge that links Mn(1) to Mn(3) and Mn(4) renders Mn(1) coordinatively saturated in the absence of hydration, whereas in structures type **I** ('Berlin-like') and **II** ('Hyogo-like') there is a vacant hydration site on Mn(1).

*Structure type **I***: In structure $\mathbf{I}^-$, the addition of seven H_2O ligands does not saturate any of the 'available' metals Mn(1), Mn(3), Mn(4), or Ca. Mn(1) and Mn(3) are not hydrated at all, whereas Mn(4) and Ca each pick up only one water ligand. Instead, the majority of the added water molecules coordinate through hydrogen bonding with each other, with the skeletal carboxylate bridges between metal atoms, or with the two metal-coordinated water ligands. This paucity of metal-based water-ligand coordination can be rationalized by the overall low charge state of the cluster, with an oxidation state pattern of $Mn^{III}Mn^{III}Mn^{III}Mn^{II}$. Aside from the enforced near-octahedral coordination of Mn(2), it appears that the Mn atoms prefer four- or five-coordinate geometries in this charge state. It is, however, notable that the water bound to Mn(4) is the strongest-bound of any within the complex.

In $\mathbf{I}^0$, with an oxidation-state pattern of $Mn^{III}Mn^{IV}Mn^{III}Mn^{II}$, Mn(4) and Ca are once more the only metal atoms to 'pick up' water ligands, with Mn(4) again possessing the preferred water-ligand binding site. In fact, Mn(4) has two of the three strongest H_2O-binding sites within the model, and addition of the seventh water renders Mn(4) nominally six-coordinate with three associated water ligands. In contrast to Mn(4), Ca constitutes a relatively weak hydration site, with several carboxylate O atoms identifiable as stronger anchorage points for water ligands.

In $\mathbf{I}^+$, Mn(4) is still identified as Mn^{II} (the observed oxidation-state pattern is $Mn^{III}Mn^{IV}Mn^{IV}Mn^{II}$) and is still the preferred primary position of water-ligand attachment, with the two most strongly bound water ligands within the heptahydrated model. Ca again shows a moderate tendency towards hydration, with two water ligands attached, whereas for the first time Mn(3) also accepts a water ligand to achieve octahedral coordination.

In $\mathbf{I}^{2+}$, the overall oxidation-state pattern is now $Mn^{III}Mn^{IV}Mn^{IV}Mn^{III}$. Mn(4) again has the two strongest water-ligand binding sites, whereas the site on Mn(3) is now ranked third. A relatively weak binding site on Ca is also evident, with other water molecules within the heptahydrated structure essentially occupying the second hydration sphere.

$\mathbf{I}^{3+}$ has an oxidation-state pattern of $Mn^{IV}Mn^{IV}Mn^{IV}Mn^{III}$. Again, the strongest water-ligand binding site is on Mn(4); a second site on Mn(4) is ranked fourth. The second-strongest site is that on Mn(3), whereas Ca again has a relatively weak binding site.

*Structure type **II***: The situation in structure type **II** is rather different to **I** because the distance between Mn(1) and the Mn(3)/Mn(4) μ-oxo bridge is generally larger. As a consequence, although Mn(1) is hydrated in certain charge states of structure type **II**, it does not become hydrated in any of the explored charge states for **I**. Although there is a 'pocket' between Mn(1) and the μ-oxo bridge that links Mn(3) to Mn(4) in both structure types **I** and **II**, this 'pocket' is insufficiently large in **I** to readily accommodate a water ligand. A second important structural difference between **I** and **II** is that in **II** the Mn(4) atom is too far removed from Ca to sustain a carboxylate bridge between these two metal atoms (such a bridge is a feature of both **I** and **III**): the carboxylate in question, which represents Asp170 of the WOC, tends to adopt a chelating motif in **II**, thereby occupying two coordination sites on Mn(4) rather than only one site as in **I** or **III**.

$\mathbf{II}^-$ has an oxidation-state pattern in the heptahydrate of $Mn^{II}Mn^{IV}Mn^{III}Mn^{II}$. The three most strongly bound H_2O ligands are all metal-coordinated: the strongest and the third-ranked attached to Ca, and the second-rank coordinated to Mn(4). A further, more weakly attached water ligand (ranked fifth) is also associated with the Ca, with the other water molecules hydrogen-bonded to carboxylate or oxo bridges. Despite the relative accessibility of both Mn(1) and Mn(3) in this structure type, these manganese atoms remain free of water ligands, thereby possibly reflecting their comparatively low oxidation states in this charge state.

$\mathbf{II}^0$ is unique in our study, with two quite distinct hydration patterns that exist with similar energy corresponding to $\mathbf{II}^0$ and $\mathbf{IIa}^0$ in Figure 2. The overall oxidation-state pattern is $Mn^{III}Mn^{IV}Mn^{III}Mn^{II}$. The ligation pattern is broadly similar to that for $\mathbf{II}^-$; the most strongly bound water is anchored to Ca, that to Mn(4) is fourth. The seventh water provokes an unexpected structural change, as a spontaneous proton transfer from the water strongly bound to Ca/Mn(3) converts the μ-O bridge between Mn(3) and Mn(4) to a μ-OH bridge. The free hydroxide ligand created through this proton transfer is hydrogen-bonded both to the nascent μ-OH bridge and to a water molecule now bound to Mn(1). The μ-OH-bridged structure is approximately 10 $kJ\,mol^{-1}$ lower in energy than its μ-O-bridged tautomer.

$\mathbf{II}^+$ ($Mn^{III}Mn^{IV}Mn^{III}Mn^{III}$) shows an unusually high degree of metal-centered water-ligand coordination, with three water molecules coordinated to Ca (ranked first, fourth and

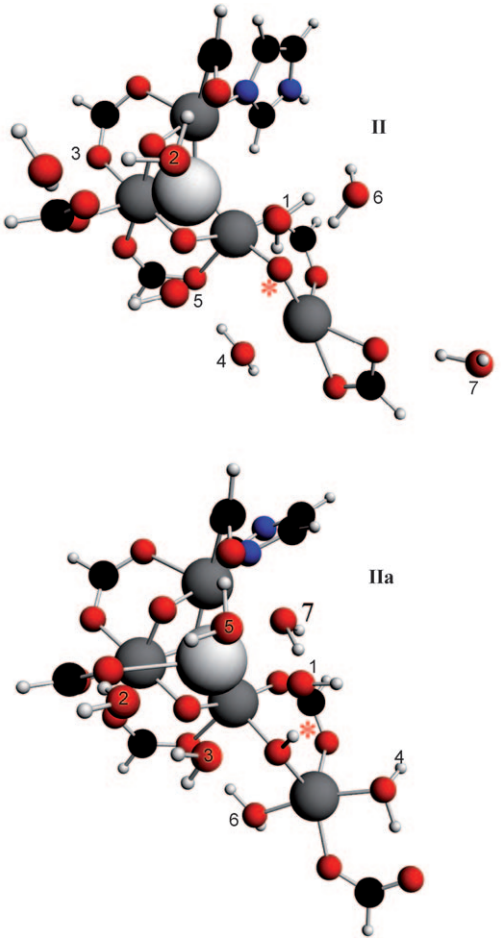

Figure 2. Structures of the lowest-energy heptahydrated complexes of two clusters **II** and **IIa**, each in the neutral charge state. Cluster **II** is the 'conventional' 'Hyogo-like' cluster analogous to that obtained at the other charge states surveyed, whereas **IIa** is a tautomer of **II** that is marginally lower in energy at higher hydration levels. The transferred proton in **IIa** converts the μ-O bridge between Mn(3) and Mn(4) to μ-OH (indicated by an asterisk). Cluster orientation is analogous to that already described for the anionic complexes in Figure 1. The diagrams are annotated with the hierarchies of water-ligand attachment, with '1' indicating the strongest-bound water ligand (or, for **IIa**, the hydroxide/proton pair that results from tautomerization).

fifth), two to Mn(4) (ranked second and fourth), and one (ranked sixth) that is nominally attached to Mn(1) (r(Mn–O) = 2.59 Å) but that is also reasonably proximate to Mn(3) (r(Mn–O) = 2.91 Å). This trend is largely repeated in $\mathbf{II}^{2+}$ (for which the oxidation-state pattern is $Mn^{III}Mn^{IV}Mn^{IV}Mn^{III}$, but with some character attributable to $Mn^{IV}Mn^{IV}Mn^{III}Mn^{III}$), with first-, second-, and sixth-ranked water ligands attached to Ca, third- and seventh-ranked water ligands anchored to Mn(4), and the fourth-ranked water ligand again shared between Mn(1) and Mn(3), but closer to Mn(3) (r(Mn–O) = 2.12 Å) than to Mn(1) (r(Mn–O) = 2.76 Å). Similarly, in $\mathbf{II}^{3+}$ ($Mn^{IV}Mn^{IV}Mn^{III}Mn^{IV}$) there are three water molecules attached to Ca (ranked first, fourth, and sixth), two to Mn(4) (second- and third-ranked), and one shared between Mn(1) (r(Mn–O) = 2.12 Å) and Mn(3) (r(Mn–O) = 2.71 Å).

In the cationic charge states for structure type **II**, it is notable that, although there is never formal water-ligand coordination to both Mn(1) and Mn(3), there is consistently one water molecule shared between these two Mn atoms. Further, throughout all of the charge states explored, one of the water ligands associated with Ca is always between 3.3 and 3.5 Å away from Mn(3). This contrasts with the situation observed for structure type **I**, in which Ca coordination of water ligands does not occur in an orientation that confers reasonable proximity to Mn(3). As shown in the discussion to follow, the more accessible 'cleft' region between the Ca, Mn(1), and Mn(3) atoms unique to structure type **II**, has important ramifications for substrate water binding.

*Structure type **III***: In $\mathbf{III}^{-}$ (oxidation-state pattern $Mn^{III}Mn^{IV}Mn^{II}Mn^{II}$ but with some $Mn^{III}Mn^{III}Mn^{III}Mn^{II}$ character), metal-centered hydration occurs at Ca (second- and fourth-ranked H_2O ligands), Mn(4) (third-ranked), and Mn(3) (seventh-ranked). Hydration of Mn(4) (strongest-bound) and Ca (second- and fourth-ranked) persists in $\mathbf{III}^{0}$ ($Mn^{III}Mn^{IV}Mn^{III}Mn^{II}$), but there is no water attachment evident to Mn(3) in this charge state. A greater propensity for metal-based coordination is evident for $\mathbf{III}^{+}$, with all of the top five water-ligation sites being metal-centered: Mn(4) (first, fifth), Ca (second, third), and Mn(3) (fourth). This pattern is repeated almost exactly the same for $\mathbf{III}^{2+}$, which again has two water ligands attached to Mn(4), two to Ca, and one to Mn(3) within the top-six-ranked water molecules. Finally, in $\mathbf{III}^{3+}$ the metal-based water-binding site preferences are to Mn(3) (first), Mn(4) (second), and then Ca (fourth, seventh).

Quantitative estimation of water-ligand binding energies: If the active water ligands are metal-centered, then there exists no more than six feasible binding-site pairs among the range of structures surveyed here: Mn(4)/Mn(4), Mn(4)/Ca, Ca/Ca, Mn(3)/Ca, Mn(1)/Ca, or Mn(1)/Mn(3). Of these possibilities, the strongest-binding pairs are typically Mn(4)/Mn(4), Mn(4)/Ca, and Ca/Ca. However, it is not at all clear that the active water binding sites are necessarily the strongest-binding sites within the complex.

In Table 6, we report the ranked hydration bond-dissociation energies across the ranges of structure type and charge state examined. Identification is also reported, where appropriate, of the metal-centered water-ligand bond strengths. Note that the reported bond strengths are for the attachment of isolated water ligands to minimal-size models of the presumed PSII active site,[28] for which the bond strength of the nth water molecule to cluster $\mathbf{I}^{q+}$ is determined as shown in Equation (1):

$$D(\mathbf{I}^{q+}\cdot[H_2O]_{n-1}\cdots H_2O) = E(\mathbf{I}^{q+}\cdot[H_2O]_{n-1}) + E(H_2O) - E(\mathbf{I}^{q+}\cdot[H_2O]_{n}) \quad (1)$$

Table 6. Cluster-model hydration bond-dissociation energies (in kJ mol^{-1}) as a function of charge state q, hydration number n, and structure type. Figures in brackets are for **II*** charge-compensated structures (see text).

q[a]	n[b]	D[**I**···$(H_2O)_n$][c]	M[d]	D[**II**···$(H_2O)_n$][c]	M[d]	D[**III**···$(H_2O)_n$][d]	M[d]
−1	1	78	Mn(4)	108 (82) (s)[g]	Ca	45	
	2	63		45 (38)	Mn(4)	65	Ca
	3	32		56 (62)	Ca	37	Mn(4)
	4	35		47 (42)		46	Ca
	5	45	Ca	39 (50)	Ca	36	
	6	30		38 (21)		43	
	7	38		29 (8) (f)		35	Mn(3)
0	1	60	Mn(4)	≈186[h] (s)	Mn(1,3)	50	Mn(4)
	2	51		65	Ca	43	Ca
	3	56	Mn(4)	63		49	
	4	33		51	Mn(4)	44	Ca
	5	44		53	Ca	48	
	6	28	Ca	31	Mn(4)	37	
	7	24		23 (f)	Mn(1)	20	
1	1	87	Mn(4)	89 (s)	Ca	72	Mn(4)
	2	80	Mn(4)	84	Mn(4)	58	Ca
	3	50		60		53	Ca
	4	50	Ca	55	Ca	47	Mn(3)
	5	32		39	Ca	59	Mn(4)
	6	45	Mn(3)	29 (f)	Mn(1)[e]	39	
	7	33	Ca	29	Mn(4)	35	
2	1	126	Mn(4)	98 (65)	Ca	92	Mn(4)
	2	88	Mn(4)	82 (105) (s)	Ca	83	Ca
	3	76	Mn(3)	89 –	Mn(4)	73	Mn(3)
	4	70	Ca	62 (7) (f)	Mn(3)[f]	73	Mn(4)
	5	66		58 (53)		68	
	6	65		58 (37)	Ca	60	Ca
	7	51		42 (54)	Mn(4)	36	
3	1	160	Mn(4)	118	Ca	136	Mn(3)
	2	110	Mn(3)	107	Mn(4)	116	Mn(4)
	3	91		105	Mn(4)	105	
	4	90	Mn(4)	91	Ca	92	Ca
	5	81		72		89	
	6	74	Ca	56	Ca	74	
	7	57		81	Mn(1)[e]	72	Ca

[a] Charge state. [b] Hydration number. [c] Bond strength for ligation of the nth water molecule, obtained as (for example) $E(\mathbf{I}^{q+}\cdot[H_2O]_{n-1}) + E(H_2O) - E(\mathbf{I}^{q+}\cdot[H_2O]_n)$. [d] Metal atom identified as binding site for the nth water ligand. [e] Mn(1) is closest metal atom, although Mn(3) is also within 3.0 Å of the O atom of the water ligand. [f] Mn(3) is the closest metal atom, although Mn(1) is also within 3.0 Å of the O atom of the water ligand. [g] s, f indicate suggested slow- and fast-exchanging substrate water molecules, respectively. See text. [h] Calculated for removal as OH^- (see text) and with application of a solvent correction determined using the conductor-like screening model (COSMO) solvent correction ($\varepsilon = 78.4$).

Other effects, such as the influence of possible steric crowding that arises from the surrounding protein structure, remain to be assessed, and will be explored in detail in future work.

Proton transfer in structure type II: As discussed below, structure **II** has features that are particularly congruent with the functional enzyme state. In particular, we regard the $\mathbf{II}^0$ proton-transfer effect described earlier as highly significant in the context of the experimental water-exchange kinetics. Consequently, we have performed additional calculations on a structure, $\mathbf{II}^0$*, which is a charge-neutralized version of $\mathbf{II}^-$ that contains an additional proton located on the μ-O bridge between Mn(3) and Mn(4) (see Figure 3 and Table 6). This was motivated by the observation that the S-state proton-release pattern[29,30] and electrochromic studies[29] indicate a charge-conserving $S_0 \rightarrow S_1$transition. The preferred oxidation-state pattern for $\mathbf{II}^0$*, $Mn^{III}Mn^{III}Mn^{III}Mn^{II}$, is also one of the dominant oxidation-state patterns found for (nonprotonated) $\mathbf{II}^-$. Also, a water molecule is now weakly associated with Mn(1), as is found for $\mathbf{II}\,\mathbf{a}^0$ (see Figure 4).

Analogous to $\mathbf{II}^0$, we have also undertaken calculations on a $\mathbf{II}^{+}$* species (see Figure 5), which is a charge-compensated (deprotonated) version of $\mathbf{II}^{2+}$, to addresses the known charge neutrality of the $S_2 \rightarrow S_3$ transition.[29,30] Deprotonation of $\mathbf{II}^{2+}$ is most readily effected by removal of a proton from the water strongly bound to Mn(4), thereby resulting in an oxidation-state pattern for the $\mathbf{II}^{+}$* structure of $Mn^{III}Mn^{IV}Mn^{III}Mn^{IV}$. Interestingly, the latest 2.9 Å XRD data locates a Cl^- ion (seen also at lower resolution by Br^- substitution)[31] and possibly an adjacent water molecule on the opposite side of the cluster from Ca and Y_z. The position of this water molecule is approximately equivalent to the water molecule on Mn(4), which is seen in all S states only for structure **II** (see Figures 3–Figure 6) with a binding energy of 40–90 kJ mol^{-1} (see Table 6). This correspondence makes the above deprotonation of the Mn(4)-bound water ligand a mechanistically attractive feature given that the Cl^- ion is known to be functionally necessary[32] and is located near the entrance of a channel, thus connecting the WOC to the lumen, which is thought to be associated with proton rather than water movement.[7,31] Most mechanistic considerations, which assign important roles to Ca and Y_z in the O–O bond-formation reaction, would argue against the water at this binding site being one of the substrate water molecules.

Comparison of experimental data with computational structures: There are several laboratory data sets relevant to substrate–water interaction with the Mn/Ca site. These include: 1) S-state-dependent water-exchange kinetics;[33] 2) magnetic coupling of the WOC to isotopically labeled water (for S_0 and S_2 states);[34–36] and 3) FTIR measurements on WOC interactions with isotopically labeled substrate water (for S_1 and S_2 states).[37,38] We briefly summarize the experimental

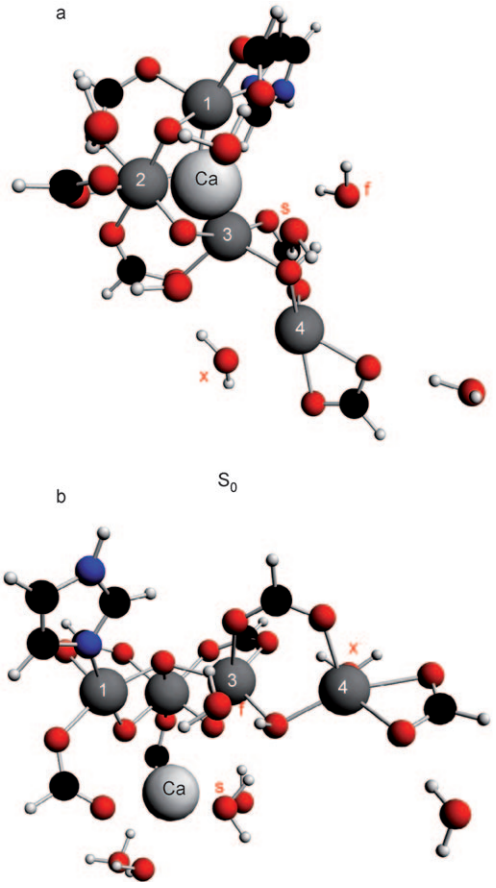

Figure 3. Structure of heptahydrated $\mathbf{II}^{0}$*, which corresponds (see text) to our expected WOC structure in S_0. Two approximately orthogonal views are provided of the same structure. Mn atoms are labeled 1 to 4. Water ligands are labeled as 'f' and 's,' which correspond to the expected identities of the 'fast' and 'slow'-exchanging substrate water ligands, and as 'x,' which denotes the water ligand tentatively identified in the latest 2.9 Å XRD structure.

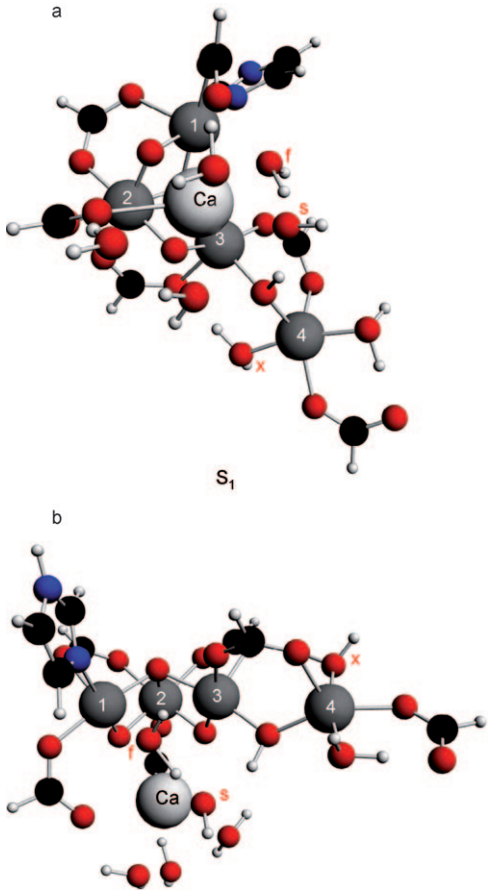

Figure 4. Structure of heptahydrated $\mathbf{IIa}^{0}$, which corresponds to our S_1 model of the WOC. Atom labeling and orientation of the views presented are consistent with that adopted in Figure 3.

results and discuss their implications for the computational structures presented here.

Water exchange: Hillier and Wydrzynski[33] have studied substrate water exchange kinetics for all stable S states of the WOC (see Table 7). Two exchanging sites, one 'fast' and one 'slow,' are identified. We have previously shown[39,40] that, for S_0 through to S_3, the slow exchange kinetics imply simple, unimolecular rate-determining steps, for example, debinding from the catalytic site, and therefore the observed Arrhenius activation energy should reflect the true debinding energy. The fast exchange process is consistent (at least in S_3) with 'single-file' diffusion through a proteinaceous pore. These fast kinetics carry no 'memory' of the actual binding site, which must have substantially lower binding energy ($<60\,kJ\,mol^{-1}$) for the substrate water than that associated with the slow site, assuming the same channel provides external water access to both sites.

Table 7. Substrate water-exchange rates in WOC.[a]

S state	Slow water		Fast water	
	k_{ex} [10 °C, s^{-1}][b]	E_a [$kJ\,mol^{-1}$][c]	k_{ex} [10 °C, s^{-1}][b]	E_a [$kJ\,mol^{-1}$][c]
S_0	10–20[d]	–	>100	–
S_1	2.2×10^{-2}	86±10	>100	–
S_2	2.2	75±10[e]	>175	–
S_3	2.1	75±10[e]	37±2	≈40±5

[a] Data from ref. [33]. See also ref. [39]. [b] First-order exchange rate constant at 10 °C. [c] Apparent activation energy. [d] Range for $^{34}O_2$ and $^{36}O_2$ detected rates. See ref. [33]. [e] Average for S_2 and S_3 combined data.

A remarkable feature of the substrate water-exchange kinetics is the near constancy of the slow rate across S_0, S_2, and S_3. The apparent H_2O-binding energy in S_2 and S_3 is approximately $75\,kJ\,mol^{-1}$. The rate slows over a hundredfold in S_1, with a corresponding increase of around $10\,kJ\,mol^{-1}$ in the apparent binding energy. This trend is counterintuitive as one would expect the rates to systematically decline as the Mn cluster is progressively oxidized and protons are lost through the S-state cycle. The pattern suggests that the slow water is bound at a site not progressively altered throughout the S cycle, but reversibly modified in S_1. Our results provide a natural candidate for this site that not only rationaliz-

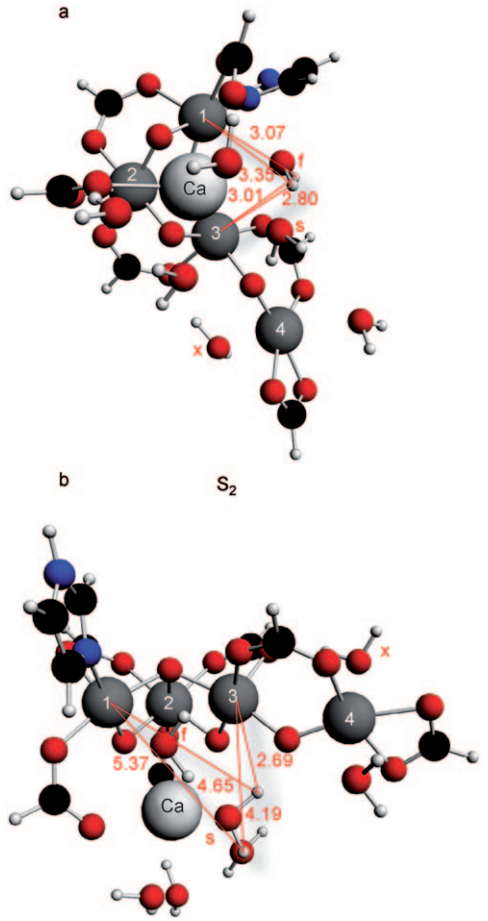

Figure 5. Structure of heptahydrated $\mathbf{II}^{+}$, which corresponds to our S_2 model of the WOC. Atom labeling and orientation of the views presented are consistent with that adopted in Figure 3. a) H–Mn distances for the proposed 'fast' substrate water ligand are shown; b) the corresponding 'slow' substrate water distances are shown. The two 'fast' water Mn(1)–deuteron distances are close to the values determined from the two strong couplings seen in ^{2}H ESEEM for the S_2 state in Table 8 (assuming $\rho_1 \approx 2$, see text). Magnetic interactions with Mn(3) would be weak if $\rho_3 \approx 0$ (see text).

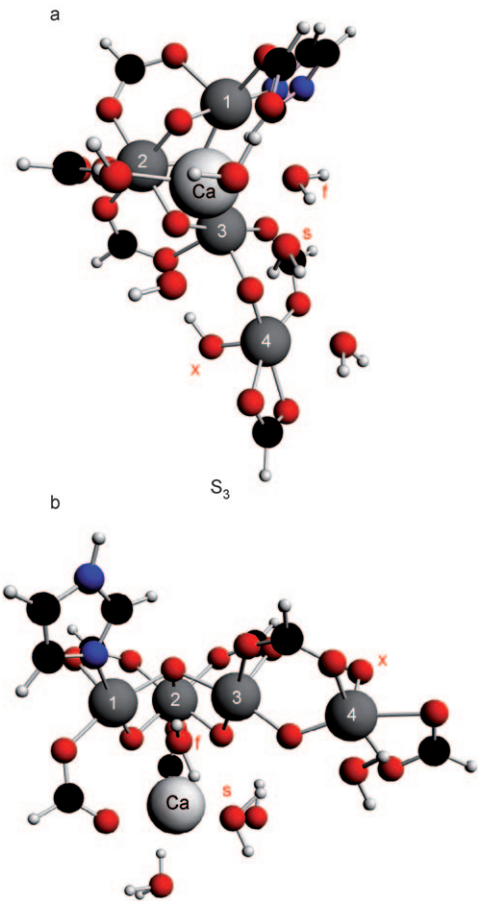

Figure 6. Structure of heptahydrated $\mathbf{II}^{+}$*, which corresponds to our S_3 model of the WOC. Atom labeling and orientation of the views presented are consistent with that adopted in Figure 3.

es the exchange kinetics but is also consistent with the substrate–water interactions with the cluster inferred from both the electron spin-echo envelope modulation (ESEEM) and FTIR studies discussed below. Alone of the three structure types, structure **II** possesses a water-accessible 'cleft' region between Mn(1), Ca, and Mn(3). Two water/hydroxide ligands may be accommodated in this cleft throughout the S state cycle, if the charge-neutralized version ($\mathbf{II}^{0}$*) of this structure is assigned to S_0 (see Figures 3–6). One water molecule, generally the strongest or second-strongest ligated water, is predominantly bound to Ca (see Table 6) but distantly bridges to Mn(3), approximately aligned along its Jahn–Teller axis (the Mn(3) oxidation state remains constant at +3 between $\mathbf{II}^{-}$ and $\mathbf{II}^{+}$*). This water also hydrogen bonds with the μ-oxo bridge between Mn(3) and Mn(4). As discussed earlier, proton transfer from this water to the oxo bridge occurs in S_1, triggered by Mn(2) oxidation, which reverses in S_2 when Mn(4) is oxidized. Formally, this water is hydroxide in S_1 (see Figure 4). The other water molecule that can be accommodated in the cleft is weakly bound between Mn(1) and Mn(3), again approximately aligned along their Jahn–Teller axes.

In S_0, S_2, and S_3, the more strongly ligated water molecule in the cleft, which is associated mainly with Ca, is bound with near constant energy at (93 ± 12) kJ mol^{-1} (see Table 6) based on our calculation of progressive hydration energies. For the lower-energy, proton-transferred form of S_1 (i.e., $\mathbf{II}\,\mathbf{a}^{0}$), this method is more problematic: the precise pathway by which the substrate 'debinds' (sequential, concerted, or intermediate between these) hugely influences the computed energy change (30–170 kJ mol^{-1}). However, it is reasonable that this water, now formally OH^{-}, cannot debind in a fully concerted manner, so its activation barrier for exchange is likely to be significantly above that in the other S states, in which it binds and displaces as the neutral species. Thus, we suggest that this water (or hydroxide) is the slowly exchanging substrate species in the protein in all S states. Its computed binding energy (as water) is approximately 15 kJ mol^{-1} above that inferred experimentally, but this is hardly surprising as our calculations are for a situation under vacuum, with no corrections for the protein environ-

ment. Application of solvent corrections, in single-point calculations summarized in Table S32 (see the Supporting Information) systematically reduce the 'slow' ligand-binding energy values, but reinforce the near-constancy of the 'slow' values for S_0, S_2, and S_3, across a range of dielectric constant values ((64 ± 4) kJ mol^{-1} for $\varepsilon=5.0$, (61 ± 4) kJ mol^{-1} for $\varepsilon=10.0$, (58 ± 5) kJ mol^{-1} for $\varepsilon=78.4$). Although the absolute H_2O-binding values from these solvent-corrected calculations are uniformly lower than expected for the true protein, these results are highly encouraging for the interpretation of structure type **II** as a minimum-complexity model of the true PSII active site.

Substrate interaction with Mn probed by electron paramagnetic resonance (EPR): The S_0 and S_2 states of the Mn cluster are spin half states at low temperature, with broad Mn hyperfine structured signals ('multilines') amenable to pulsed EPR study. Nuclear couplings to Mn from labeled water species (^2H_2O, $H_2{}^{17}O$) are observed in ESEEM[34,35] and hyperfine sublevel correlation experiments (HYSCORE)[41] and from H_2O protons in electron nuclear double resonance (ENDOR).[36,42] The most recent ^{2}H ESEEM study by Åhrling et al.[35] of substrate–water interaction with the Mn cluster in the S_0 and S_2 states involved 'physiological' flash advanced functional turnover. This study identified a minimum set of three deuteron/Mn-coupling classes, assigned to substrate D_2O–Mn interactions, which were very similar in all S_0 and S_2 samples. A variable population of D–Mn couplings was also seen, most likely due to exchangeable protons in the protein matrix near the Mn cluster.

An effective Mn−D distance may be estimated from the ESEEM data, if the deuteron is assumed to be interacting mainly with a single Mn center, the spin projection, ρ, of which in the coupled cluster is known. Estimates of the ρ_i values have been proposed from the modeling of multiline EPR signals,[39,43,44] but now direct estimates are possible from a combination of recent experimental results and our cluster calculations. The observed ^{14}N histidine couplings on the S_2 multiline signal, in both the native system and the D1-D170H mutant (see the Supporting Information), suggest that ρ_1 is large (≈2) for Mn(1) and ρ_4 small (≈0) for Mn(4). Since the ρ_i values must sum to unity, $\rho_2+\rho_3$ must be approximately -1. Furthermore, recently reported ENDOR studies of ^{13}C-labeled D1-A344 (see the Supporting Information) suggest that ρ_2 is approximately -1, so ρ_3, like ρ_4, is small. Table 8 summarizes results from the D_2O ESEEM data, interpreted as above, for the three consistent Mn–D coupling classes, assuming $|\rho|=1$ or 2 for the ligating Mn. The two strong single couplings are thoroughly determined by the ESEEM experiments but modeling of the four weakly coupling deuterons is only approximate.

The protons from the 'slow' water are not likely to be those most strongly coupled magnetically to the cluster in S_2 (or S_0). One proton is approximately 2.7 Å from Mn(3), but the other is over 4 Å away from any Mn. The other water molecule present in the cleft, the computed binding energy of which is generally <60 kJ mol^{-1} (consistent with the fast exchanging substrate water), has protons sufficiently close to Mn(1) for strong magnetic coupling in S_2 (or S_0). In fact, the S_2 distances (Figure 5) are within around 0.1 Å of those inferred experimentally (Table 8), assuming $\rho_1\approx2$. This is a strongly suggestive result, given that Mn(1) is the only magnetic ion in the cluster that could significantly interact with these water deuterons due to distance or projection factor effects. Therefore, qualitatively, we have assigned the two strong substrate water proton couplings to the likely 'fast' exchanging water bound between Mn(1) and Mn(3). Proton(s) on the 'slow' water and also the water bound to Mn(4) then contribute to the weak couplings in Table 8 as they are all near Mn ions with low ρ values.

Table 8. Mn-exchangeable ^{2}H couplings from ESEEM measurements on S_2 and S_0 states of PSII.

Deuteron class	No. of deuterons	Mn,^{2}H coupling [MHz][a]	r_i [Å][b,c] $\lvert\rho\rvert=2$	r_i [Å][b,c] $\lvert\rho\rvert=1$
		S_2 state		
1	1	0.93 ± 0.05	2.97	2.36
2	1	0.65 ± 0.03	3.34	2.65
3	≈0–10[d]	0.44 ± 0.03	3.7	2.9
4	4	0.25 ± 0.05	4.6	3.7
		S_0 state		
1	1	0.90 ± 0.05	3.00	2.38
2	1	0.58 ± 0.05	3.47	2.76
3	≈5–8[d]	0.42 ± 0.05	3.9	3.1
4	4	0.25 ± 0.05	4.6	3.7

[a] Average ^{2}H dipole hyperfine interactions from modeling of flash turnover Mn ESEEM data, with/without MeOH; spinach PSII. Results from ref. [35]. [b] Mn–deuteron point dipole distance assuming Mn ρ value indicated (see text). [c] Uncertainty <0.05 Å for a given ρ value for classes 1 and 2. [d] Full range of deuterons for both flash and 200 K turnover samples.

Substrate interaction with the WOC probed by FTIR: Nogouchi and co-workers have extensively examined the WOC by FTIR difference spectroscopy. Using H^2- and O^{18}-labeled water, they have shown that one water molecule, very probably a substrate species, binds to the WOC in the S_1 and S_2 states, with substantially inequivalent hydrogen-bonding interactions for the two protons.[37] One water proton is strongly hydrogen-bonded (not detected) to some nearby base and the other only weakly hydrogen-bonded (or not at all). One interpretation of the small ^{2}H downshift effects and the large (31 cm^{-1}) upshift of the weakly hydrogen-bonded proton on the $S_1\rightarrow S_2$ transition is that the inequivalence of the hydrogen bonding in the target water is reduced in S_2 relative to S_1.

The 'fast' water described above is also a likely candidate for the species identified in the FTIR experiments.[37,38] In $\mathbf{II}\,\mathbf{a}^0$ (i.e., S_1; see Figure 4), this water molecule makes one strong hydrogen bond to the adjacent OH^-, which we infer to be the Ca-associated 'slow' exchanging substrate water, whereas the other hydrogen atom of the 'fast' water has no intermolecular connections in our model systems. In $\mathbf{II}^+$ (S_2; see Figure 5), the OH^- group becomes H_2O and the hydrogen bond between this newly protonated species and the above 'fast' water ligand weakens, thereby reducing the in-

equivalence of the OH bonds of the latter. This is at least qualitatively consistent with the pattern seen in FTIR spectra for the OH stretch of the presumed substrate–water species. Furthermore, recent mutation studies on Glu354 of the CP43 peptide in PSII indicate that the water in question is associated with a Mn that Glu354 ligates.[38] This is consistent with the type **II** structural model in which the carboxylate ligand modeling Glu354 bridges the Mn(2) and Mn(3) centers.

Overview: The above picture is quite different from that proposed elsewhere. Much of the emphasis in the theoretical investigations by other groups[13–27] has focused on Mn(4), generally regarded as the most coordinatively unsaturated Mn atom within the PSII active site. Our own calculations confirm that for structures **I** and **III**, Mn(4) is almost always the metal site with the strongest water-binding energies, regardless of cluster charge state. For structure **II**, however, one water molecule is always strongly bound to Mn(4) (near the water site located in the most recent XRD structure),[7] but the highest-affinity water site is generally that bridging Ca and Mn(3). Neither structure **I** or **III** offers an obvious candidate for the slow-exchanging substrate water in terms of an S-state binding energy pattern such as that seen for structure **II**. For structure **I**, the affinity pattern for the strongest-binding water (associated with Mn(4)) is essentially the opposite to that which is required, that is, weakest for $q=0$ (proposed S_1). For structure **III**, the waters are generally too weakly bound up to $q=2$ (proposed S_3) to be consistent with the exchange kinetics energies. The situation is not resolved by shifting the assumed oxidation pattern for the cluster, that is, taking $q=1$ to be S_0, as the binding energies then just monotonically increase with the S state.

In summary, several specific features of structure **II** and the oxidation-state assignment proposed here ($q=0$ for S_1, and so on) provide a natural 'fit' to the water-exchange, deuteron-coupling, and FTIR data discussed above. These key features are the 'openness' of structure **II**, which allows the coordination of two water molecules in the cleft formed between Mn(1), Ca, and Mn(3), the near-constancy of the chemical environment of the 'slow' water, and its propensity for hydrogen bonding and reversible proton transfer to the Mn(3)–Mn(4) μ-oxo bridge. All of these features are specifically contingent on the metal/oxo connectivity of structure **II**, namely, that the Mn(3)–Mn(4) oxo bridge connects only these metals and does not bridge to the Ca or Mn(1) (as occurs in structures **I**, **III**, and the QM/MM model[24] of the London structure). The consequent 'isolation' of Mn(4) results in the carboxylate that represents Asp 170 becoming bidentate towards Mn(4), rather than bridging between Mn(4) and Ca (as in **I** and implied by the most recent crystal structures,[6,7] although an earlier version[4] indicated that it was bidentate).

We suspect that the structural changes between the protein that adopts the metal/ligand arrangements in structures **I** or **II** could be the basis of the apparent heterogeneity of the magnetic hyperfine coupling observed in the S_2 state. Studies in which the S_2-state multiline is generated by low-temperature (200 K) continuous illumination from the dark-adapted S_1 state are variable, often lacking detectable ESEEM coupling to deuterons from exogenous D_2O in a significant fraction of centers that appear to be 'dry.'[35,45] A similar effect appears to have been seen in the recent HYSCORE study of PSII using $H_2{}^{17}O$.[41] In contrast, measurements that involve 'physiological' flash-advanced samples lacked this variability. These observations can be straightforwardly rationalized if it is assumed that the 'dry centers' correspond to more Berlin-like **I** structures in which the cleft region between Mn(1), Ca, and Mn(3) is too tight to accommodate the second (fast) water molecule responsible for the strong couplings to Mn(1). Apparently, these centers can still advance by redox accumulation, at least initially, to higher S states.

Because the water-exchange and ^{2}H ESEEM studies (Tables 7 and 8) involved fully functional turnover states, we suggest that structure **II** is actually closest to the active enzyme site of those possibilities examined here. Interestingly, the occurrence of reversible substrate-water proton transfer to an oxo bridge, as the basis of the anomalous slow water-exchange kinetics pattern, has been previously proposed.[39] In that study, it was suggested that this could represent a pathway for coupled electron proton transfer during the catalytic O–O bond-formation step in S_4. Thus, the proton on the oxo bridge that we suggest is actually present in S_0 (i.e., the $\mathbf{II}^0$* state) arises from this transfer in the previous turnover cycle of the functional system.

In this proposal for the functional enzyme state, only three water molecules actually bind at or near Mn throughout the whole cycle. These are the two substrate waters bound in the cleft formed between Mn(1), Ca, and Mn(3), and the water on Mn(4), which probably corresponds to the putative water resolved in the latest XRD structure. A second water molecule sometimes associated with Mn(4) (see the Supporting Information) for structure **II** is actually very weakly bound and can be removed with no significant change to the results. Thus, six waters 'satisfy' the cluster; three on Ca, two roughly shared between Ca and Mn(1)/Mn(3) (the substrate waters), and one totally on Mn(4). The latter deprotonates in S_3 for charge balance, which the adjacent Cl^- ion possibly facilitates. This is totally consistent with the known phenomenology of Cl^- removal[32], which permits advancement to a (perturbed) S_2 state but blocks advancement of the Mn cluster to S_3.

The results presented here further support our assignment of the general oxidation state levels in the functional WOC. Thus, S_0 is formally $(Mn^{III})_3Mn^{II}$, or equivalent ('low-oxidation-state paradigm'), with subsequent states obtained by electron removal. This assignment is not new;[40,43] but more recently the alternative S_0 pattern $(Mn^{III})_3Mn^{IV}$ ('high-oxidation-state paradigm') has been favored[46,47] in experimental studies (and in all quantum chemical studies by other research groups).[13–27] Support for the 'high-oxidation-state paradigm' derives principally from an analysis of the observed Mn X-ray absorption near-edge structure (XANES)

edge energies for the resolved S_0 to S_3 states of flash-advanced PSII, using a comparison set of Mn oxide/carbonate compounds of well-defined mean redox state.[46] We have recently addressed the question theoretically by using a newly developed methodology based on time-dependent DFT, applied initially to a series of known Mn model compounds.[48,49] The results for PSII will be presented separately;[58] but it is already clear that inorganic oxides may not provide a sufficiently close chemical analogy to permit the reliable interpretation of Mn oxidation levels in PSII from the observed XANES energies.

Computational Methods

Density functional theory calculations employed the Amsterdam Density Functional (ADF) program, version ADF 2006.01, developed by Baerends et al.[50–52] Calculations were run in parallel mode with the AlphaSever supercomputer housed at the ANU Supercomputer Facility and operated under the Australian Partnership for Advanced Computing.

Geometry optimizations, in C_1 symmetry, used the gradient algorithm of Versluis and Ziegler[53] and featured convergence constraints (energies to within 0.5 mhartree, gradient and radial convergence to within 0.005) twice as tight as the ADF default values. Electrons in orbitals up to and including 1s (C, N, O) or 2p (Mn) were treated in accordance with the frozen-core approximation. All calculations were performed in an unrestricted fashion.

Functionals used in the calculations were the local density approximation (LDA) to the exchange potential, the correlation potential of Vosko, Wilk, and Nusair (VWN),[54] and the nonlocal corrections of Becke[55] and Perdew.[56] The (Slater-type orbital) basis sets used were generally of triple-ζ-plus-polarization quality (TZP), although some single-point calculations (at the BP/TZP optimized geometries) were additionally performed at the BP/TZ2P (triple-ζ-plus-two polarization functions) and BP/QZ4P (quadruple-ζ-plus-four polarization functions) levels of theory, for benchmarking purposes. Comparison of the BP/TZP, BP/TZ2P, and BP/QZ4P relative energies for trihydrated structure types **I**, **II**, and **III** across the range of charge states $q=-1$ to $+3$ (see Table S31 in the Supporting Information) shows agreement between the three levels of theory to within $\pm 6\,\mathrm{kJ\,mol^{-1}}$, thereby indicating that the smaller TZP basis set is adequate to accurately describe the Mn_4-containing structures of interest across the relevant distribution of charge states.

Solvent corrections, for example using a polarized continuum model (PCM), were not routinely applied. It is not clear that the overlay of solvent corrections is appropriate on a structure for which up to seven discrete water molecules have been explicitly included, and in any event the dielectric constant ε within the PSII solvent sheath is not reliably determined. Within the reasonably constrained confines of the WOC and its immediate environs, the aqueous contribution is arguably better modeled as a network of hydrogen-bonded water ligands (as we have done) than as an effectively idealized enveloping solvent. Nonetheless, a series of solvent-corrected single-point calculations were pursued, at representative dielectric constant values of $\varepsilon=5.0$, 10.0, and 78.4, on the lowest-energy structures of the WOC model set $\mathbf{II}^{0}$*, $\mathbf{II}^{0}$, $\mathbf{II}^{+}$, and $\mathbf{II}^{+}$* across the range of hydration values $n=0$ to 7 (see Table S32 in the Supporting Information). These results are discussed within the text.

The model structures used in these calculations corresponded to the general formula $[CaMn_4C_9H_{10}N_2O_{16}]^{q+}\cdot(H_2O)_i$ ($q=-1$, 0, 1, 2 3; $i=0$–7) in which the amino acid residues (Ala344, Asp170, Asp342, Glu189, Glu333, Glu354, His332) directly coordinated to the Mn_4Ca cluster in the WOC were replaced with simple carboxylate and imidazole groups. Preliminary optimizations on these structures were performed in the fully ferromagnetically coupled, all-high-spin $S_{max}=(16-q)/2$ spin state. Optimized S_{max} geometries were reoptimized in a 'broken symmetry' (BS) configuration[57] with the spin polarization on sequential Mn atoms as 'ABAB.' This configuration has $|M_S|=(0, 1/2, \text{or } 1)$ depending on the oxidation states of the respective Mn atoms. These calculations were employed to determine the preferred sites of hydration for $[CaMn_4C_9H_{10}N_2O_{16}]^{q+}\cdot(H_2O)_3$ as follows. The heptahydrated structure $[CaMn_4C_9H_{10}N_2O_{16}]^{q+}\cdot(H_2O)_7$ was characterized with initial placement of water ligands at all nominally 'free' sites on the Mn(1), Mn(3), Mn(4), and Ca atoms, so as to allow coordinative saturation of all metal atoms in the hydrated structure, and the fully dehydrated $[CaMn_4C_9H_{10}N_2O_{16}]^{q+}$ geometry from this calculation was then itself optimized. Then, individual water molecules at the positions determined from the $[CaMn_4C_9H_{10}N_2O_{16}]^{q+}\cdot(H_2O)_7$ calculation were added to the optimized $[CaMn_4C_9H_{10}N_2O_{16}]^{q+}$ structure; these monohydrated structures were themselves optimized, and a determination of the next preferred water-binding site at each hydration level was built up incrementally. This lengthy computational strategy was judged the most appropriate method by which to ensure that the most stable $[CaMn_4C_9H_{10}N_2O_{16}]^{q+}\cdot(H_2O)_i$ structures ($i=0$–7) could be characterized at each charge state.

Conclusion

In the calculations reported here, we have explored the consequences of sequential hydration (up to 7 water ligands) on our series of Mn_4Ca structure types across charge states from $q=-1$ to $q=+3$, which correspond to a formal oxidation-state assignment of $(Mn^{III})Mn^{II}$ for S_0, up to $(Mn^{IV})_3Mn^{III}$ for S_4. We have also explored charge-compensated structures for which the overall charge on the cluster is maintained at $q=0$ or $+1$, consistent with the experimental data on sequential proton loss in the real system. These calculations strengthen many of the assertions established in our earlier investigation of the trihydrated structures. The preference among virtually all structures is for antiferromagnetic coupling with the Mn^{II} and Mn^{III} atoms invariably adopting high-spin configurations regardless of whether or not ferromagnetic or antiferromagnetic coupling is constrained. Energy differences between the various structure types remain sufficiently small that, mindful of the limitations of the models, none of the three structure types can be excluded as a possible PSII active-site model on the basis of the calculated relative energies alone. Oxidation-state patterns across the Mn atoms and the preferred mode of antiferromagnetic coupling both tend to be sensitive to subtle geometric differences between the three structure types, and also the degree of hydration. Across most charge states, the oxidation state adopted by Mn(2) is Mn^{IV}, whereas Mn(4) is generally the manganese atom most likely to persist as Mn^{II} as the charge state is ramped up.

Six to seven water molecules are generally required to fully hydrate all the structures studied and, of these, three or four water molecules are directly associated with Ca. For all three structure types, hydration at Mn(4) and Ca is possible and in general these correspond to the strongest water-binding sites. Hydration at Mn(2) cannot occur as it is coordinatively saturated in all three structure types. Hydration at Mn(1) or Mn(3) is dependent on the geometry of the metal-atom cluster. In structure type **III**, the presence of an additional tri-μ-oxo bridge, which links Mn(1) to Mn(3) and Mn(4), renders Mn(1) coordinatively saturated in the absence of hydration. In both structure types **I** and **II**, there is

a plausible hydration site on Mn(1), but for **I** this site is not occupied in any of the charge states as the 'pocket' between Mn(1) and the μ-oxo bridge that links Mn(3) to Mn(4) is insufficient to accommodate a water ligand. The situation is different for structure type **II**, for which the distance between Mn(1) and the Mn(3)/Mn(4) μ-oxo bridge is generally larger than in **I**. As a consequence, although there is never a water ligand coordinated to both Mn(1) and Mn(3) in structure **II**, there is consistently one water shared between these two Mn atoms. Furthermore, in all explored charge states for structure **II**, one of the water ligands associated with Ca is always between 3.3 and 3.5 Å away from Mn(3).

When the fully hydrated structures are considered in light of the experimental water-exchange kinetics and substrate-binding interactions, as revealed by EPR and FTIR with labeled water species, one type clearly suggests itself as most consistent with the data. This is the 'open' structure type **II**, which possesses a water-accessible 'cleft' region between Mn(1), Ca, and Mn(3) that is capable of accommodating two water/hydroxide ligands throughout the S-state cycle. These, we suggest, are the two substrate–water sites in PSII. The structure permits substrate-proton interaction with the most EPR-sensitive portions of the cluster and provides a natural explanation for the unusual pattern of S-state-dependent 'slow-site' water-exchange kinetics not possible for structure types **I** and **III**. Our preferred model also provides a simple rationalization for the positions of the newly located water molecule and Cl^- ion in the most recent XRD structure. Finally, because the water-exchange and ESEEM studies involved fully functional turnover states of PSII, we conclude that structure **II** is actually closest to the active enzyme site of those possibilities examined here.

Acknowledgements

R.S. and R.J.P. gratefully acknowledge financial assistance from the Australian Research Council. The authors also acknowledge the generous provision of supercomputing time on the platforms of the NCI (National Computational Infrastructure) Facility in Canberra, Australia, which is supported by the Australian Commonwealth Government. R.J.P. dedicates this paper to the memory of a close colleague and friend, Mike Evans (1940–2007), in whose laboratories at University College London the D_2O ESEEM measurements on flash-advanced PSII were carried out.

[1] *Photosystem II: The Light-Driven Water: Plastoquinone Oxidoreductase* (Eds.: T. Wydrzynski, K. Satoh), Springer, Dordrecht, **2005**.
[2] A. Zouni, H.-T. Witt, J. Kern, P. Fromme, N. Krauss, W. Saenger, P. Orth, *Nature* **2001**, *409*, 739–743.
[3] N. Kamiya, J.-R. Shen, *Proc. Natl. Acad. Sci. USA* **2003**, *100*, 98–103.
[4] J. Biesiadka, B. Loll, J. Kern, K.-D. Irrgang, A. Zouni, *Phys. Chem. Chem. Phys.* **2004**, *6*, 4733–4736.
[5] K. N. Ferreira, T. M. Iverson, K. Maghlaoui, J. Barber, S. Iwata, *Science* **2004**, *303*, 1831–1838.
[6] B. Loll, J. Kern, W. Saenger, A. Zouni, J. Biesiadka, *Nature* **2005**, *438*, 1040–1044.
[7] A Guskovl, J. Kern, A. Gabdulkhalov, M. Broser, A. Zouni, W. Saenger, *Nat. Struct. Mol. Biol.* **2009**, *16*, 334–342.
[8] See, for example: K. Sauer, J. Yano, V. K. Yachandra, *Coord. Chem. Rev.* **2008**, *252*, 318–335.
[9] J. Yano, J. Kern, K.-D. Irrgang, M. J. Latimer, U. Bergmann, P. Glatzel, Y. Pushkar, J. Biesiadka, B. Loll, K. Sauer, J. Messinger, A. Zouni, V. K. Yachandra, *Proc. Natl. Acad. Sci. USA* **2005**, *102*, 12047–12052.
[10] S. Petrie, R. Stranger, P. Gatt, R. J. Pace, *Chem. Eur. J.* **2007**, *13*, 5082–5089.
[11] S. Petrie, R. Stranger, R. J. Pace, *Chem. Eur. J.* **2008**, *14*, 5482–5494.
[12] P. E. M. Siegbahn, *Q. Rev. Biophys.* **2003**, *36*, 91–145.
[13] M. Lundberg, P. E. M. Siegbahn, *Phys. Chem. Chem. Phys.* **2004**, *6*, 4772–4780.
[14] P. E. M. Siegbahn, M. Lundberg, *Photochem. Photobiol. Sci.* **2005**, *4*, 1035–1043.
[15] P. E. M. Siegbahn, M. R. A. Blomberg, *Philos. Trans. R. Soc. London Ser. A* **2005**, *363*, 847–860.
[16] P. E. M. Siegbahn, M. Lundberg, *J. Inorg. Biochem.* **2006**, *100*, 1035–1040.
[17] P. E. M. Siegbahn, *Chem. Eur. J.* **2006**, *12*, 9217–9227.
[18] P. E. M. Siegbahn, *Philos. Trans. R. Soc. London Ser. B* **2008**, *363*, 1221–1228.
[19] P. E. M. Siegbahn, *Inorg. Chem.* **2008**, *47*, 1779–1786.
[20] P. E. M. Siegbahn, *Dalton Trans.* **2009**, 5832–5840.
[21] J. P. McEvoy, J. A. Gascon, V. S. Batista, G. W. Brudvig, *Photochem. Photobiol. Sci.* **2005**, *4*, 940–949.
[22] E. M. Sproviero, J. A. Gascon, J. P. McEvoy, G. W. Brudvig, V. S. Batista, *J. Inorg. Biochem.* **2006**, *100*, 786–800.
[23] E. M. Sproviero, J. A. Gascon, J. P. McEvoy, G. W. Brudvig, V. S. Batista, *J. Chem. Theory Comput.* **2006**, *2*, 1119–1134.
[24] E. M. Sproviero, J. A. Gascon, J. P. McEvoy, G. W. Brudvig, V. S. Batista, *J. Am. Chem. Soc.* **2008**, *130*, 3428–3442.
[25] E. M. Sproviero, J. A. Gascon, J. P. McEvoy, G. W. Brudvig, V. S. Batista, *J. Am. Chem. Soc.* **2008**, *130*, 6728–6730.
[26] E. M. Sproviero, J. P. McEvoy, J. A. Gascon, G. W. Brudvig, V. S. Batista, *Photosynth. Res.* **2008**, *97*, 91–114.
[27] M. Kusunoki, *Biochim. Biophys. Acta Bioenerg.* **2007**, *1767*, 484–492; M. Kusunoki, *Biochim. Biophys. Acta Bioenerg.* **2008**, *1777*, 477.
[28] In PSII itself, the water ligands that attach are presumed to do so from a reservoir of available water within the structural void of the protein's central cavity, with ligated and 'free' water molecules within this cavity likely all connected through one or more concatenated hydrogen-bond networks. Water ligation likely involves an adjustment in the hydrogen bonding of the ligated water molecule to its neighbors, an effect that is ignored in our calculations.
[29] F. Rappaport, J. Lavergne, *Biochim. Biophys. Acta* **2001**, *1503*, 246–259.
[30] H. Suzuki, M. Sugiura, T. Noguchi, *J. Am. Chem. Soc.* **2009**, *131*, 7849–7857.
[31] J. W. Murray, K. Maghlaoui, J. Kargul, N. Ishida, T.-L. Lai, A. W. Rutherford, M. Sugiura, A. Boussac, J. Barber, *Energy Environ. Sci.* **2008**, *1*, 161–166.
[32] C. F. Yocum, *Coord. Chem. Rev.* **2008**, *252*, 296–305.
[33] W. Hillier, T. Wydrzynski, *Biochim. Biophys. Acta Bioenerg.* **2001**, *1503*, 197–209.
[34] M. C. W. Evans, J. H. A. Nugent, R. J. Ball, I. Muhiuddin, R. J. Pace, *Biochemistry* **2004**, *43*, 989–994.
[35] K. A. Åhrling, M. C. W. Evans, J. H. A. Nugent, R. J. Ball, R. J. Pace, *Biochemistry* **2006**, *45*, 7069–7082.
[36] D. R. Britt, K. A. Campbell, J. F. Peloquin, M. L. Gilchrist, C. P. Aznar, M. M. Dicus, J. H. Robblee, J. Messinger, *Biochim. Biophys. Acta Bioenerg.* **2004**, *1655*, 158–171.
[37] T. Noguchi, M. Sugiura, *Biochemistry* **2000**, *39*, 10943–10949.
[38] Y. Shimada, H. Suzuki, T. Tsuchiya, T. Tomo, T. Noguchi, M. Mimuro, *Biochemistry* **2009**, *48*, 6095–6103.
[39] R. J. Pace, K. A. Åhrling, *Biochim. Biophys. Acta Bioenerg.* **2004**, *1655*, 172–178.
[40] D. Kuzek, R. J. Pace, *Biochim. Biophys. Acta Bioenerg.* **2001**, *1503*, 123–137.

[41] J.-H. Su, W. Lubitz, J. Messinger, *J. Am. Chem. Soc.* **2008**, *130*, 786–787.
[42] H. Yamada, H. Mino, S. Itoh, *Biochim. Biophys. Acta Bioenerg.* **2007**, *1767*, 197–203.
[43] T. G. Carrell, A. M. Tyryshkin, G. C. Dismukes, *J. Biol. Inorg. Chem.* **2002**, *7*, 2–22.
[44] J. M. Peloquin, K. A. Campbell, D. W. Randall, M. A. Evanchik, V. L. Pecoraro, W. H. Armstrong, D. R. Britt, *J. Am. Chem. Soc.* **2000**, *122*, 10926–10942.
[45] M. C. W. Evans, A. M. Rich, J. H. A. Nugent, *FEBS Lett.* **2000**, *477*, 113–117.
[46] H. Dau, P. Liebisch, M. Haumann, *Anal. Bioanal. Chem.* **2003**, *376*, 562–583.
[47] L. V. Kulik, B. Epel, W. Lubitz, J. Messinger, *J. Am. Chem. Soc.* **2007**, *129*, 13421–13435.
[48] A. R. Jaszewski, R. Stranger, R. J. Pace, *J. Phys. Chem. A* **2008**, *112*, 11223–11234.
[49] A. R. Jaszewski, R. Stranger, R. J. Pace, *Phys. Chem. Chem. Phys.* **2009**, *11*, 5634–5642.
[50] Amsterdam Density Functional v.2006.01 S.C.M., E. J. Baerends, J. Autsbach, A. Bérces, F. M. Bickelhaupt, C. Bo, P. M. Boerrigter, L. Cavallo, D. P. Chong, L. Deng, R. M. Dickson, D. E. Ellis, M. v. Faassen, L. Fan, T. H. Fischer, C. Fonseca Guerra, S. J. A. van Gisbergen, J. A. Groeneveld, O. V. Gritsenko, M. Gruning, F. E. Harris, P. van den Hoek, C. R. Jacob, H. Jacobsen, L. Jensen, G. van Kessel, F. Kootstra, E. van Lenthe, D. A. McCormack, A. Michalak, J. Neugebauer, V. P. Osinga, S. Patchkovskii, P. H. T. Philipsen, D. Post, C. Pye, W. Ravenek, P. Ros, P. R. T. Schipper, G. Schreckenbach, J. G. Snijders, M. Sola, M. Swart, D. Swerhone, G. te Velde, P. Vernooijs, L. Versluis, O. Visser, F. Wang, T. A. Wesolowski, E. van Wezenbeek, G. Wiesenekker, S. K. Wolff, T. K. Woo, A. L. Yakovlev, T. Ziegler, Theoretical Chemistry, Vrije Universiteit, Amsterdam, http://www.scm.com.
[51] C. F. Fonseca Guerra, J. G. Snijders, G. te Velde, E. J. Baerends, *Theor. Chem. Acc.* **1998**, *99*, 391–403.
[52] G. te Velde, F. M. Bickelhaupt, E. J. Baerends, C. Fonseca Guerra, S. J. A. van Gisbergen, J. G. Snijders, T. Ziegler, *J. Comput. Chem.* **2001**, *22*, 931–967.
[53] L. Versluis, T. Ziegler, *J. Chem. Phys.* **1988**, *88*, 322–328.
[54] S. H. Vosko, L. Wilk, M. Nusair, *Can. J. Phys.* **1980**, *58*, 1200.
[55] A. D. Becke, *Phys. Rev. A* **1988**, *38*, 3098–3100.
[56] J. P. Perdew, *Phys. Rev. B* **1986**, *33*, 8822.
[57] L. Noodleman, *J. Chem. Phys.* **1981**, *74*, 5737–5743.
[58] A. Jaszewski, R. Pace, R. Stranger, unpublished results.

Received: April 29, 2010
Published online: October 22, 2010

